Measurement of the $t\bar{t}Z$ production cross section in the three lepton final state with 13.0 fb^{-1} of $\sqrt{s} = 8$ TeV pp collision data collected by the ATLAS detector

by

Arash Khazraie Zamanpour

B.Sc., University of Toronto, 2010

A THESIS SUBMITTED IN PARTIAL FULFILLMENT OF
THE REQUIREMENTS FOR THE DEGREE OF

MASTER OF SCIENCE

in

The Faculty of Graduate Studies

(Physics)

THE UNIVERSITY OF BRITISH COLUMBIA

(Vancouver)

December 2012

Abstract

A measurement of the $t\bar{t}Z$ production cross section with the ATLAS detector in pp collisions at the LHC is presented. The search is performed on 13.0 fb^{-1} of data collected in 2012. Only final states with three leptons are considered, in which the Z boson decays to a pair of leptons and one of the W bosons coming from $t \to bW$ decays gives rise to a lepton after decay. An excess of 8.95 $\pm$ 0.62 (stat) $^{+0.37}_{-0.59}$ (sys) events above background is observed with a significance of 3.64 standard deviations above zero. We have assumed no statistical error on the acceptance or efficiency of detection. In the trilepton channel, a direct measurement of the $t\bar{t}Z$ production cross section of $\sigma_{t\bar{t}Z} = 254 \pm 104$ (stat) $\pm$ 19 (sys) fb is obtained.

Table of Contents

List of Tables

List of Figures

Acknowledgements

The work presented in this thesis could not have been achieved without the help of my advisors Anadi Canepa and Colin Gay. I am thankful for their guidance and support, and appreciate the flexibility they gave me in letting me pursue my interests. A special thanks goes out to Zoltan Gecse, Sam King, Chang-Wei Loh, Matthew Gignac and Kyle Boone for the countless times you helped me with coding.

Dedication

To my parents and my brother.

Chapter 1

Introduction

The large mass of the top quark and coupling to the Higgs boson of order 1 suggests that it could play an important role in EW symmetry breaking (EWSB). New physics related to the EWSB may be found via top quark precision observables. One possible signal for new physics is deviations of the $tt\gamma$, ttZ and ttW couplings from the values predicted by the Standard Model (SM). Although the top quark was discovered more than fifteen years ago [2, 3], most of its properties are still not well known [4]. For instance, the couplings of the top quark to the electroweak (EW) gauge bosons, in particular the Z boson, have not been directly measured. These couplings can also take different values in some of beyond the Standard Model (BSM) models, such as technicolor [5] or Little Higgs models [6] . In many beyond standard model searches, as for example SUSY, the $t\bar{t}Z$ is a potential background. Therefore, it is important to measure its cross section.

There is yet no direct evidence of top quarks coupling to the Z boson, although there have been strong indirect bounds on this coupling from LEP precision data [7].

The ttZ coupling could not be constrained via measuring the $t\bar{t}$ production at hadron colliders with intermediate virtual Z bosons, due to the fact that the cross section for $pp \to t\bar{t}$ is mainly dominated by processes with only QCD couplings. Coupling of the ttZ production may be constrained via searches for direct production of $t\bar{t}$ in association with a Z boson. This process had a very low cross section at the Tevatron. Its cross section was measured in the trilepton final state at 0.02 fb [7]. This is a very low cross section therefore the process can only be observed at the LHC.

The ATLAS collaboration has placed a 95% credibility upper limit of 0.71 pb on the cross section of $t\bar{t}Z$ production using a Bayesian prescription [8] with 4.7 fb^{-1} of $\sqrt{s} = 7$ TeV pp collision data collected.

The CMS collaboration recently presented a preliminary measurement of the $t\bar{t}Z$ cross section [9], finding $\sigma_{t\bar{t}Z} = 0.30^{+0.14}_{-0.11}$ (stat) $^{+0.04}_{-0.02}$ (syst) pb with a significance of 3.66 standard deviations from the background only hypothesis.

Chapter 2

Theoretical Overview

2.1 The Standard Model of Particle Physics

The Standard Model (SM) of particle physics is a Quantum Field Theory (QFT) of electromagnetic (EM), weak, and strong interactions. SM is a theory based on a SU(3)⊗SU(2)⊗U(1) local gauge symmetry which describes the interactions between fundamental particles by the exchange of gauge bosons.

From the gauge symmetry SU(2)⊗U(1) and the mechanism of spontaneous symmetry breaking [10], one can define gauge bosons (W^+, W^- and Z) as mediators of the weak interaction, the photon (γ) of the electromagnetic interactions, and a new particle called the Higgs boson. The SU(2)⊗U(1) gauge group does not incorporate the mass terms for the gauge bosons or fermions without breaking the gauge invariance. When this symmetry is broken to $U(1)_{QED}$, it gives mass to the three electroweak gauge bosons while keeping the photon massless by leaving the electromagnetic symmetry $U(1)_{QED}$ unbroken.

The gauge symmetry can be extended to SU(3)⊗SU(2)⊗U(1) to include the strong interactions mediated by eight coloured massless gluons. This is an exact symmetry that couples three different colour charges ("red", "green" and "blue") carried by the 6 quarks and 8 gluons. The gluons carry both a colour and an anticolour charge.

All matter consists of quarks and leptons which are elementary fermions. A fermion can be an elementary or compound particle with half-integer spin ($\frac{1}{2}$, $\frac{3}{2}$,...) while a boson has integer spin (0, 1, ...).

Quarks cannot exist freely due to the fact that only colour neutral states are observed in nature. This is referred to as the "confinement" of quarks. There are three generations of quarks discovered so far. Leptons also come in three generations.

In the SM, charged current processes change the lepton or quark flavour. This is done according to the weak eigenstates which are different from their mass eigenstates. They are transformed by applying a rotation described by

Particle	symbol	EM charge	Weak charge (isospin)	Strong charge (colour)	Mass [MeV]
fermions					
electron	e	-1	-1/2	0	0.511
electron neutrino	ν_e	0	+1/2	0	$\leq 50\times10^{-6}$
muon	μ	-1	-1/2	0	105.6
muon neutrino	ν_μ	0	+1/2	0	≤ 0.5
tau	τ	-1	-1/2	0	1776.8
tau neutrino	ν_τ	0	+1/2	0	≤ 70
up	u	+2/3	+1/2	R/G/B	~ 2.3
down	d	-1/3	-1/2	R/G/B	~ 4.8
charm	c	+2/3	+1/2	R/G/B	~ 1275
strange	s	-1/3	-1/2	R/G/B	~ 95
top	t	+2/3	+1/2	R/G/B	$\sim 173.5\times10^3$
bottom	b	-1/3	-1/2	R/G/B	~ 4180
bosons					
photon	γ	0	no	no	0
Z	Z	0	yes	no	91.187×10^3
W	$W^\pm$	±1	yes	no	80.39×10^3
gluon	g	0	no	yes	0
Higgs	H^0	0	yes	no	$\geq114\times10^3$

Table 2.1: Particles of the standard model.

the Cabbibo-Kobayashi-Maskawa (CKM) mixing matrix V_{CKM}[11]:

$$\begin{pmatrix} d' \\ s' \\ b' \end{pmatrix} = V_{CKM} \begin{pmatrix} d \\ c \\ b \end{pmatrix} \tag{2.1}$$

$$V_{CKM} = \begin{pmatrix} V_{ud} & V_{us} & V_{ub} \\ V_{cd} & V_{cs} & V_{cb} \\ V_{td} & V_{ts} & V_{tb} \end{pmatrix} = \begin{pmatrix} 0.974 & 0.225 & 0.003 \\ 0.225 & 0.973 & 0.041 \\ 0.009 & 0.040 & 0.999 \end{pmatrix} \tag{2.2}$$

where $d^{'}$, $s^{'}$ and $b^{'}$ are the weak eigenstates and the corresponding mass eigenstates are d, s and b.

The PMNS matrix, or lepton mixing matrix is the analogue of the CKM matrix describing the mixing of leptons.

Table 2.1 lists the standard model particles with names, symbols, mass and different charges. For the fermions, these charges are quantum numbers

defining their interactions. Masses are listed in MeV, 10^6 electron volts. The value of one electron volt, eV, is the amount of energy gained by the charge of a single electron moved across an electric potential difference of one volt.

The Lagrangian of the SM is required to be local, gauge-invariant and renormalizable. It can be divided into four pieces:

$$\mathcal{L}_{SM} = \mathcal{L}_{Matter} + \mathcal{L}_{Gauge} + \mathcal{L}_{Yukawa} + \mathcal{L}_{Higgs}. \tag{2.3}$$

The matter part, given by:

$$\begin{aligned}\mathcal{L}_{Matter} = \bar{Q}^i_L i\gamma^\mu D_\mu Q^i_L + \bar{u}^i_R i\gamma^\mu D_\mu u^i_R + \bar{d}^i_R i\gamma^\mu D_\mu d^i_R \\ + \bar{L}^i_L i\gamma^\mu D_\mu L^i_L + \bar{e}^i_R i\gamma^\mu D_\mu e^i_R,\end{aligned} \tag{2.4}$$

contains the kinetic energy of the fermions and their interactions with the gauge fields. Q^i_L and L^i_L are the quark and lepton doublets, where i represents a sum on the generations.
The Gauge part, given by:

$$\mathcal{L}_{Gauge} = -\frac{1}{2}Tr\mathbf{G}^{\mu\nu}\mathbf{G}_{\mu\nu} - \frac{1}{8}Tr\mathbf{W}^{\mu\nu}\mathbf{W}_{\mu\nu} - \frac{1}{4}B^{\mu\nu}B_{\mu\nu}, \tag{2.5}$$

contain the kinetic energy of the gauge fields and their self interactions. $\mathbf{G}^{\mu\nu}$, $\mathbf{W}^{\mu\nu}$ and $B^{\mu\nu}$ above are the gluon, weak and hypercharge field-strength tensors.
The Yukawa interaction of the Higgs field with the fermions, given by:

$$\mathcal{L}_{Yukawa} = -\Gamma^{ij}_u \bar{Q}^i_L \epsilon \phi^* u^j_R - \Gamma^{ij}_d \bar{Q}^i_L \phi d^j_R - \Gamma^{ij}_e \bar{L}^i_L \phi e^j_R + h.c., \tag{2.6}$$

where Γ_u, Γ_d, Γ_e are 3×3 complex matrices that result in the mixing between different fermion generations.
Finally, the Higgs part, written as:

$$\mathcal{L}_{Higgs} = (D^\mu \phi)^\dagger D_\mu \phi + \mu^2 \phi^\dagger \phi - \lambda(\phi^\dagger \phi)^2, \tag{2.7}$$

where

$$D_\mu = (\partial_\mu + ig_S \mathbf{G}_\mu + \frac{ig}{2}\mathbf{W}_\mu + \frac{ig'}{6}B_\mu). \tag{2.8}$$

In the Higgs Lagrangian λ describes the Higgs self-coupling and needs to be a positive real number to make the potential large as ϕ the Higgs field goes to infinity. To have a non-zero vacuum expectation value v of the Higgs field given by

$$v = \sqrt{\frac{-\mu^2}{\lambda}}, \tag{2.9}$$

the complex parameter μ needs to satisfy $\mu^2 < 0$.

This expectation value can be used to calculate the Higgs mass m_H:

$$m_H = \sqrt{\frac{\lambda}{2v}}. \tag{2.10}$$

Although the constant λ cannot be calculated, limits can be put on the mass since large masses lead to divergences in the self-coupling at a scale Λ below the Planck scale.

2.2 The Top Quark

The top quark is the heaviest particle of the six fermions in the Standard Model with a measured mass of m_t=(173.2±0.9) GeV/c^2.

In addition to its quantum numbers, its mass m_t and decay width Γ_t[12]

$$\Gamma_{LO} = \frac{G_F m_t^3}{8\pi\sqrt{2}} |V_{tb}|^2 \left(1 - \frac{M_W^2}{m_t^2}\right)^2 \left(1 + 2\frac{M_W^2}{m_t^2}\right) \tag{2.11}$$

are the most fundamental properties of the top quark. It has a very short lifetime of 0.5×10^{-24}s[13] which is about an order of magnitude smaller than the hadronization timescale. As a result it cannot form bound states before decaying to a W boson and a down-type quark. The down-type quark is almost always a bottom quark because of the large CKM matrix element $V_{tb} = 0.999152^{+0.000030}_{-0.000045}$[14].

After including higher order quantum chromodynamics (QCD) corrections, the decay width becomes:

$$\Gamma(t \to Wb) = \Gamma_{LO}\left[1 - \frac{2\alpha_s}{3\pi} f(y)\right], \tag{2.12}$$

where $\alpha_s = \frac{g_s^2}{4\pi}$ is the strong coupling constant and $f(y)$ is written as:

$$f(y) = \frac{2\pi^2}{3} - 2.5 - 3y + 4.5y^2 - 9\ln y; y = \frac{M_W^2}{m_t^2}. \tag{2.13}$$

2.3 Top Production

Top quarks are produced via both electroweak and strong interactions. In the electroweak case, a single quark is produced. There are three channels in the single top production case:

- s-channel
- t-channel
- tW channel.

In the s-channel an off-shell W boson decays into a top and a bottom quark, in the t-channel a virtual W boson transforms a bottom quark into a top quark and finally in the tW channel the top quark is produced in association with a W boson.

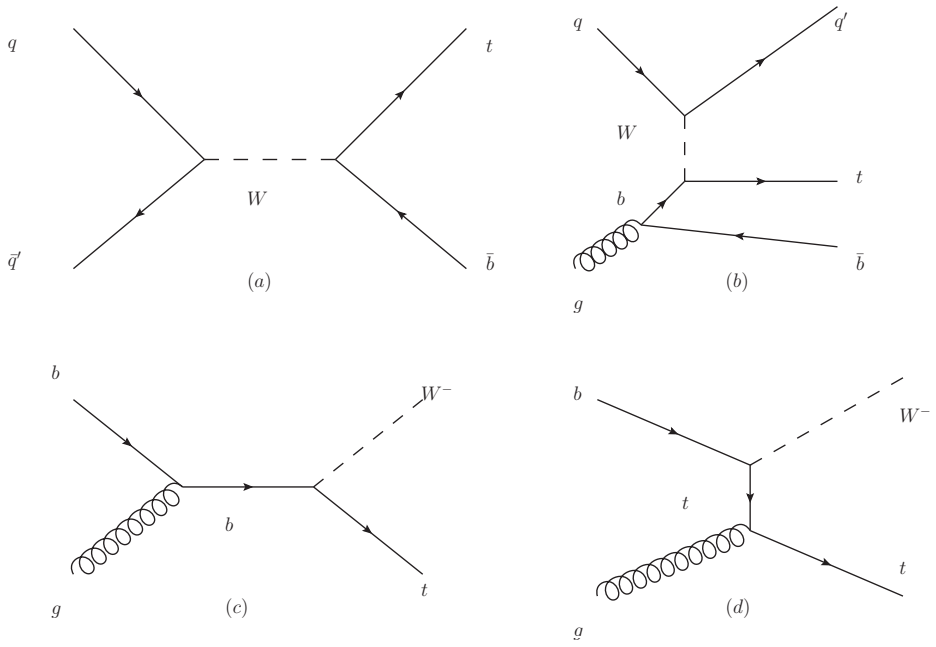

Figure 2.1: Single top production diagrams, (a) s-channel, (b) t-channel, (c) tW s-channel, (d) tW t-channel.

In proton-proton collisions, the most common production channel for top quarks is through the top and an anti-top pair production. The leading-order Feynman diagrams of $t\bar{t}$ production in gluon-gluon fusion and quark-antiquark annihilation are shown in Figure 2.2. There is also the next-to-leading order (NLO) quark-gluon that contributes to this process.

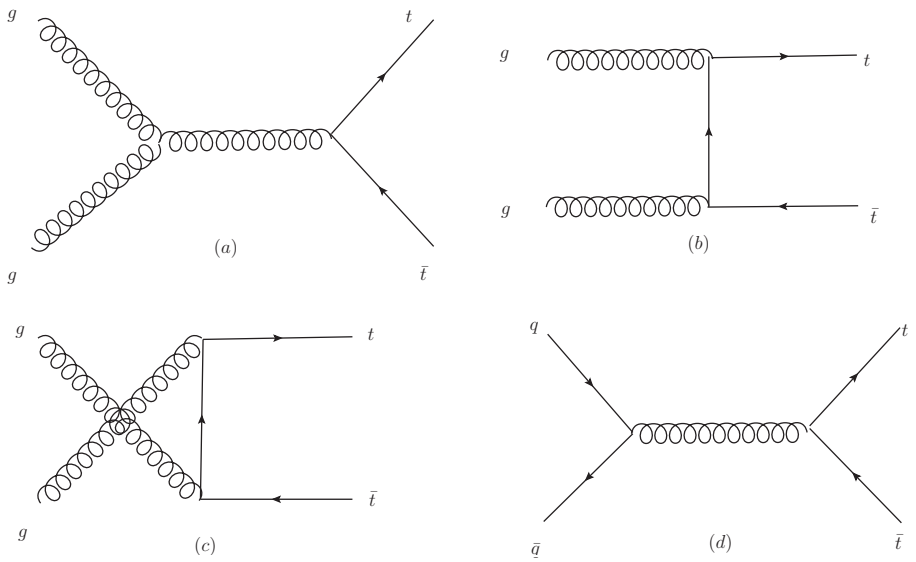

Figure 2.2: Leading order $t\bar{t}$ production diagrams: (a) s-channel, (b) t-channel, (c) u-channel, (d) $q\bar{q}$.

2.4 Production and Decay of $t\bar{t}Z$

The signal process $pp \rightarrow t\bar{t}Z$ has a theoretical cross section of $\sigma_{NLO} = 208$ fb at Next to Leading Order [15] [16]. The production diagram of the $t\bar{t}Z$ process is shown in the Figure 2.3 where a gluon decays to a $t\bar{t}$ pair along with production of a Z boson. The $t\bar{t}Z$ has the same diagrams as the $t\bar{t}$ production with the difference that a Z is emitted by one of the outgoing top quarks.

Considering leptonic decay of the Z boson (Z$\rightarrow l^+l^-$), the final topology of a $t\bar{t}Z$ event only depends on the W boson decay. The W boson could decay leptonically, W$\rightarrow l\nu_l$, or hadronically, W$\rightarrow q\bar{q}^{'}$. This gives three different decay channels:

- 4 lepton channel: this is when both W bosons decay leptonically, resulting in two high-p_T charge leptons from the W's, two leptons from the Z, and two jets from b-quark hadronization (b-jets).

- 3 lepton channel: this is when one W boson decays leptonically and the other hadronically, resulting in one high-p_T charged lepton from the W, two leptons from the Z, two b-jets and two light-flavour jets.

- 2 lepton channel: this is when both W bosons decay hadronically, giving two b-jets and four light-jets and again two leptons from the Z.

The leptonically decaying W boson can give any of the three flavours (eν_e, $\mu\nu_\mu$ or $\tau\nu_\tau$). The analysis presented in this thesis focuses on $t\bar{t}Z$ events with three leptons in the final state, resulting from decays of type $t\bar{t}(\rightarrow q\bar{q}'b\bar{b}l\nu)Z(\rightarrow ll)$, where l denotes e, μ, or a τ decaying into e or μ. The Feynman diagram for this decay channel is shown in the figure below. In this thesis no hadronically decaying τ's were considered.

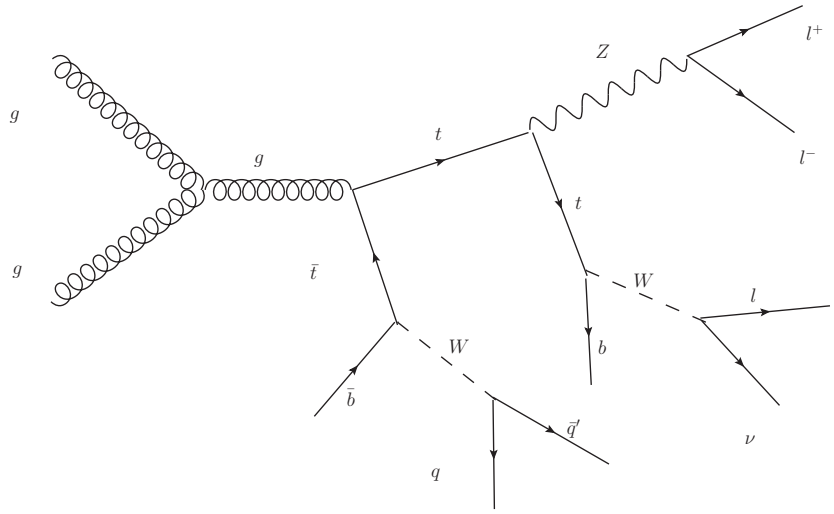

Figure 2.3: $t\bar{t}Z$ production and decay channel diagram.

2.5 The Monte Carlo Generation Method

At the LHC, proton beams are used. The proton is a baryon made of two up-quarks and one down-quark. Gluons can also split into a $q\bar{q}$ pair which can then annihilate back into a gluon and be absorbed again. These additional quark pairs in the proton are called sea quarks.

When two opposite-moving protons collide, their constituents interact in an inelastic process. The interesting collisions will give rise to new particles. Several concepts are needed to understand how a cross section at hadron colliders is determined. Among others:

• *The parton [17] distribution function (PDF):* when gluons and quarks inside two colliding protons interact, each carries a fraction of the total momentum of the original particle. The PDFs describe the probability of finding a certain quark or gluon with momentum fraction x at a given energy scale Q^2, where Q^2 is the momentum transfer from the lepton to the interacting parton. PDFs are extracted from experimental data, e.g from global fits to the data of deep-inelastic scattering experiments since they cannot be estimated with pertubative QCD.

• *The hard-process:* The interaction between two partons from the original colliding protons, if involving high Q^2, has the result to break their confinement and lead to the appearance of new particles. The products of the hard-process are usually the signature of interest. It is here that i.e. the ZZ, WZ, top quarks etc. stem from.

• *The initial state radiation (ISR):* incoming partons can radiate quarks or gluons due to quantum fluctuations. They stem from the quarks in the initial composition, and therefore will result in the loss of some of the partons initial momentum fraction and the emission of a particle.

• *The final state radiation (FSR):* similar to what happens in the case of ISR, outgoing partons radiate quarks or gluons. ISR will have momentum transfer of the order of the mass of the particle created in the collision, where FSR will have a momentum transfer lower than the mass of the particle created.

• *The underlying event:* it consists of partons from the original colliding protons that are not participating in the hard scatter. They contribute to the overall process as they hold a colour charge, but of course must become colour neutral. Usually, the underlying event shows itself through soft scatterings. The ISR/FSR processes can also be seen as part of the underlying event.

• *Pile up:* There may be more than one interaction per bunch crossing. This is called in-time pile up. If the interaction is between two protons from different bunches is called out-of-time pile up.

• *Decays:* Unstable particles like heavy hadrons or taus formed during the hard-process will decay into more stable particles after hadronisation. The decay are controlled by the branching fraction which is the likelihood of a particle decaying to a particular mode.

Chapter 3

The Experimental Setup

3.1 The Large Hadron Collider

The Large Hadron Collider, LHC is an underground particle accelerator ring with a circumference of 27 km that started operating in November 2009 facilitates probing physics at higher energies than previous accelerators.

The LHC has been designed to accelerate protons[1] to a centre-of-mass energy of $\sqrt{s} = 14$ TeV, energies 14,000 times as high as the protons have on their own. From summer 2012 LHC has operated with mean energies of 4.0 TeV per proton resulting in a centre-of-mass energy of $\sqrt{s} = 8$ TeV. The high $\sqrt{s}$ is not the only feature of the LHC. Its large instantaneous luminosity ($\mathcal{L}$), a measure of the number of collisions per unit of area and time, is designed to reach $10^{34}\text{cm}^{-2}\text{s}^{-1}$ and will allow analyses requiring many proton collisions (events) to be performed in a few years. This rate of events observed in a process under study is given by,

$$R = \epsilon\sigma\mathcal{L} \tag{3.1}$$

where σ is the cross section and ϵ the detection efficiency. The total number of events (N) is given by

$$N = \epsilon\sigma L \tag{3.2}$$

where $L = \int \mathcal{L}\text{d}t$ is the integrated luminosity. The cross section is a fixed and measurable quantity which expresses the likelihood of interaction between specific particles, while the luminosity and the efficiency are determined by the LHC and the detector respectively.

The LHC is at the end of an injection chain, a collection of accelerators and other devices that help in bringing the proton beams into collision. Before being injected into the LHC, protons are produced and then accelerated step by step up to a certain energy by a series of accelerators. This is done by introducing hydrogen gas into a Duoplasmatron device [18]. The gas held in a vacuum chamber is bombarded with electrons. The result is to

[1] The LHC can also accelerate heavy ions, but this is a different experiment and will not be discussed here.

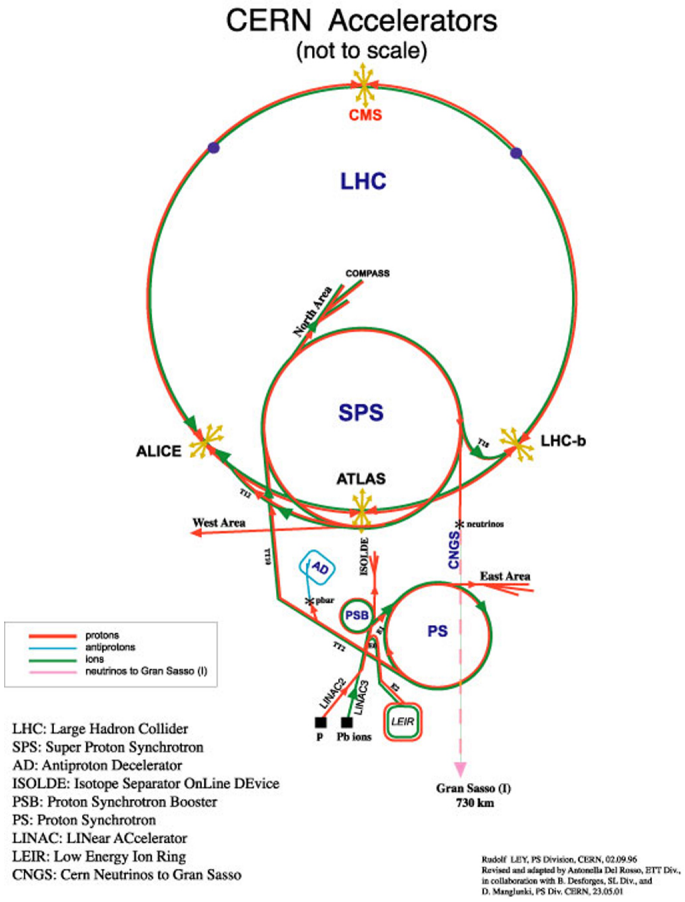

Figure 3.1: CERN accelerator complex.

ionize the gas having it in a state of plasma. Then the plasma is accelerated inside the Duoplasmatron device forming a beam. This beam is focused and then accelerated to an energy of 50 MeV in a linear accelerator, the Linac-2. The proton beam is then introduced into the Proton Synchrotron Booster (PSB). The PSB is a circular accelerator in the injection chain with four superimposed synchrotron rings. In each ring a bunch of $1.8{\times}10^{12}$ protons is formed. Here they are accelerated to an energy of 1.4 GeV subsequently.

Next accelerator is the Proton Synchrotron (PS) circular accelerator. Here the beam is accelerated to 26 GeV.

Finally, the Super Proton Synchrotron (SPS) is used to further increase

their energy to 450 GeV.

Colliding protons are grouped together into a number of bunches, each containing about 10^{11} protons. The design number of bunches is 2808, leading to interactions happening every 25 ns at nominal running and every 50 ns in the data used for this analysis.

At four points on the LHC ring, the protons from the oppositely moving beams cross and collisions occur. At these four interaction points major experiments at the LHC are situated; ALICE, ATLAS, CMS and LHC-b. The analysis presented in this thesis is performed on data collected by the ATLAS detector.

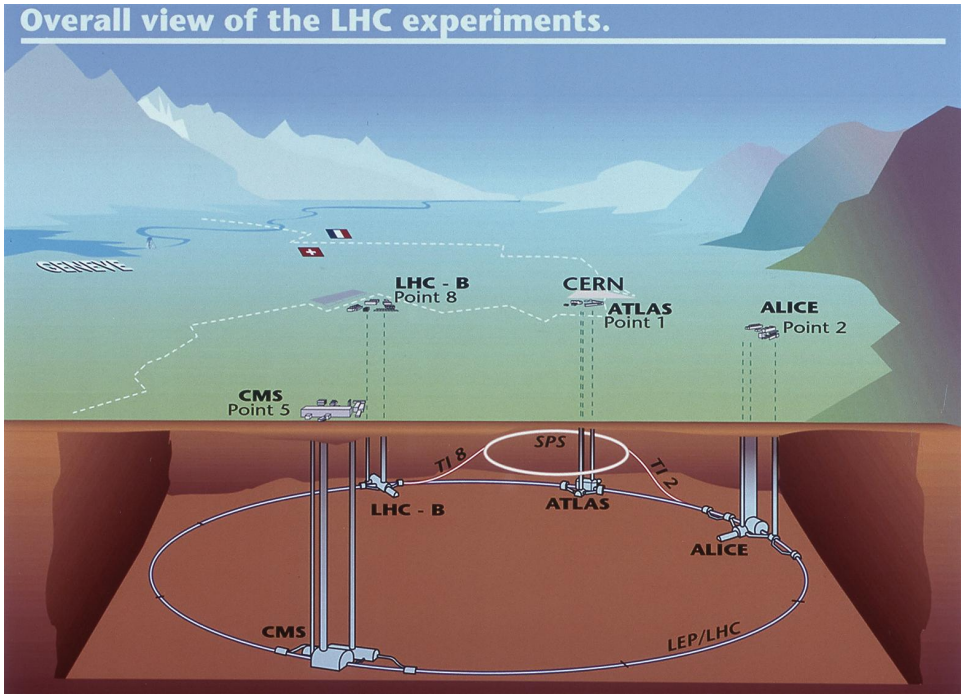

Figure 3.2: The LHC experiment.

3.2 ATLAS - A Toroidal LHC Apparatus

The ATLAS detector is a cylindrical construction of 7000 tonnes in a cavern at a depth of 100 m . With its height of 25 m and its length of 44 m, it is positioned at one of the interaction points of the LHC (Point-1). It consists

of several parts, referred to as sub-detectors, each designed and optimised for special tasks.

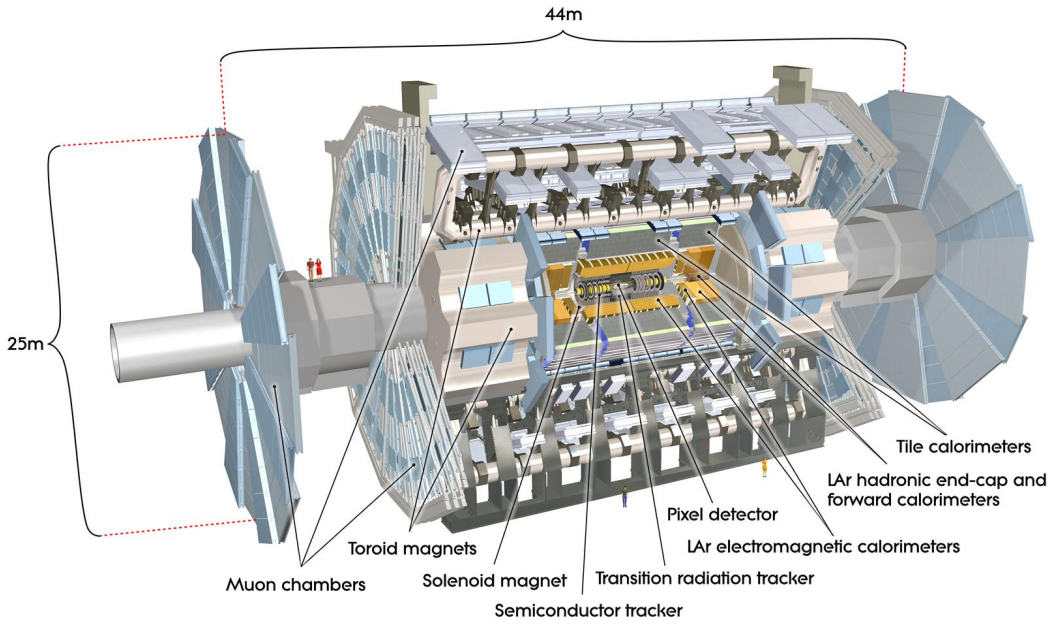

Figure 3.3: The ATLAS detector.

3.2.1 Coordinate System

- The nominal interaction point is defined as the origin of the coordinate system.
- The z-axis of the system runs parallel to the beam. The positive x-axis of the system points towards the center of the LHC and the positive y-axis points upwards towards the surface. They are perpendicular to the beam, forming a right-handed cartesian coordinate system.
- Given the cylindrical structure of the detector it is convenient to use polar coordinates. The azimuthal angle, $\phi \in [-\pi, \pi]$, is measured around the z-axis and the polar angle, $\theta \in [0, \pi]$, is measured from the z-axis.

- The polar angle runs on the xz-plane having $\theta = 0$ on the positive z-axis. For convenience this is replaced by the Lorentz invariant pseudo-rapidity (η), which is defined by:

$$\eta = -\ln\left(\tan\frac{\theta}{2}\right). \tag{3.3}$$

- The distance of two particles on the detector, the Lorentz invariant ΔR is defined as:

$$\Delta R = \sqrt{(\Delta\phi)^2 + (\Delta\eta)^2} \tag{3.4}$$

  where small values show that particles are located close to each other.

3.2.2 The Inner Detector

The Inner Detector (ID) provides the identification of charged particles and measurements of the vertex at which the hard interaction took place. It extends up to a pseudorapidity of 2.5 and it is submerged in the 2 T axial magnetic field of the solenoid superconducting magnet that surrounds it.

The ID consists of three separate sub-detector devices. Their main characteristics are summarized in Table 3.1. The Pixel detector, the Semiconductor Tracker (SCT) and the Transition Radiation Tracker (TRT) arranged into central barrel parts and two end-cap parts forming the forward detector.

Subdetector	section	Radius [cm]	Element size	Spatial resolution [μm]	Hits/track	Readout channels
Pixel		5 - 12	50 μm $\times$ 400 μm		3	80×10^6
	Barrel			10 (R-ϕ) $\times$ 115 (z)		
	End-cap			10 (R-ϕ) $\times$ 115 (R)		
SCT			80 μm		8	6×10^6
	Barrel	25 - 55		17 (R-ϕ) $\times$ 580 (z)		
	End-cap	25 - 61		17 (R-ϕ) $\times$ 580 (R)		
TRT			4 mm		30-36	3.5×10^5
	Barrel	55 - 108		130		
	End-cap	61 - 110		130		

Table 3.1: The main characteristics of the three ID subdetectors [1].

Pixel Detector

The Pixel detector is the closest to the interaction point of all the sub-detector systems. It is a silicon pixel detector with 288 modules each with

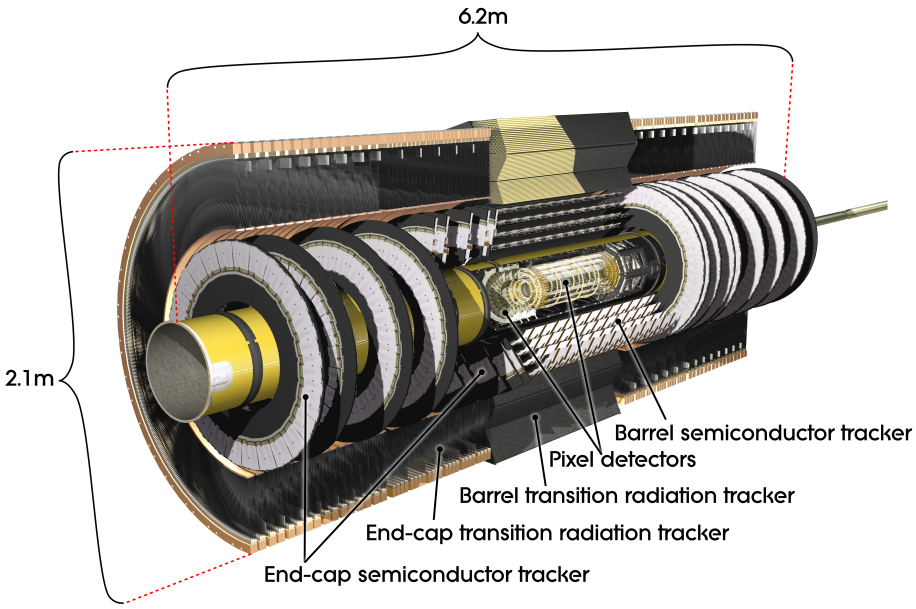

Figure 3.4: The ATLAS inner detector.

46080 pixel elements. Therefore it has a very high granularity which provides a high precision measurements of tracks as close to the interaction point as possible. The innermost layer of the Pixel detector, with a radius of about 5 cm, performs the highest precision of the reconstruction of secondary vertices that occur, for example, in decays of bottom-flavoured hadrons. The highest precision in the position measurement achieved are 10 μm in the $R - \phi$ plane and 115 μm in z-direction.

SCT

The SCT is the second element of the Inner Detectors sub-systems, going from the beam pipe outwards. It provides eight strip measurements (four space-points) for particles originating in the beam-interaction region. The SCT uses silicon microstrip technology for tracking charged particles and is constructed from silicon sensors (like the pixel detector) which are segmented in strips thus giving a position measurement. The SCT at the barrel region consists of four cylindrical shaped layers with radii of 30, 37, 44 and 51 cm of silicon strips which are arranged so that each layer has one set of silicon

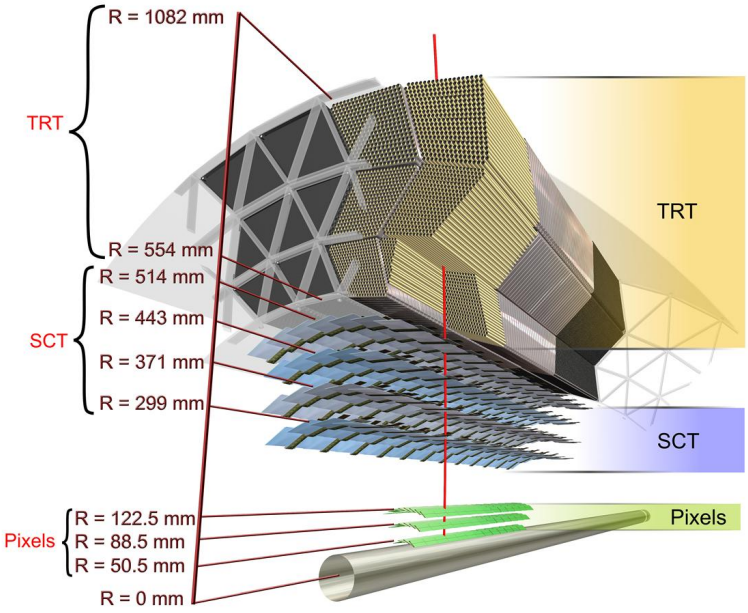

Figure 3.5: The TRT and SCT overview.

strips parallel to the beam axis and another set tilted by angle of 40 mrad in order to measure the radial and longitudinal position of the hit. With the Pixel detector, it can determine where the interaction occurred (the vertex position) and how much momentum a particle has (determined from its curvature in the magnetic field). The main difference is that instead of a pixel configuration the SCT modules follow a strip segmentation.

TRT

The TRT is the outermost system of the ID. It is a detector made from straw tubes of 4 mm diameter containing gas (a mixture of 70% Xenon, 27% Carbon dioxide and 3% Oxygen) with a wire at the centre to detect electromagnetic showers. The TRT straw layout is designed so that charged particles with transverse momentum $p_T > 0.5$ GeV and with pseudorapidity $|\eta| < 2.0$ cross typically more than 30 straws [1].

The detection is based on the ionization of the gas once a charged particle traverses it. The straw hits at the outer radius contribute significantly to the momentum measurement. It only provides $R - \phi$ information with an intrinsic accuracy of 130 μm per straw [1].

For the electron identification the TRT straws are placed inside polypropylene fibers with different refraction indices. This makes ultra-relativistic particles radiate off photons in the X-ray region. Xenon is chosen as it is sensitive to absorbing those photons resulting in massive ionisation and a much larger signal readout. The transition radiation is efficiently absorbed by the Xenon gas resulting in energy deposition of several keV in contrast to an average of 200 eV that relate with the ionization process, discriminating between the two processes.

The electron which has a small mass does emit a larger amount of radiation that allows the separation between it and heavier particles with the same momentum such as the π^+.

3.2.3 The Calorimeters

The calorimetry consists of the electromagnetic (EM) calorimeter which is nearest to the interaction point covering the region $|\eta| < 3.2$, a hadronic calorimeter covering $|\eta| < 3.2$, and forward calorimeters (FCal) extending to $3.1 < |\eta| < 4.9$. The whole system is symmetric around the beam axis and has full coverage in the ϕ direction. The EM calorimeter is used for the measurement of electrons and photons, the Hadronic calorimeter for the measurement of hadrons. A schematic view of the calorimeter system is shown in Figure 3.6. The main purpose of the calorimeters is to measure the energy of the particles and their position. The detector can measure both charged and neutral particles, through complete absorption, from a few GeV up to the TeV scale. Weakly interacting particles such as muons or neutrinos are not stopped by the Calorimeters. But muons leave a trace that can be used along with information from the Inner Detector or the Muon Spectrometer for their measurement. Nominal detector performance limits and coverage for the calorimetric system are summarized in Table 3.2.

EM Calorimeter

The EM calorimeter is a lead Liquid-Argon (LAr) detector with interlacing layers of lead and stainless steel. Lead has a short radiation length which means electrons or photons moving through the calorimeter will shower and create a large number of photons within short distances. The Argon will

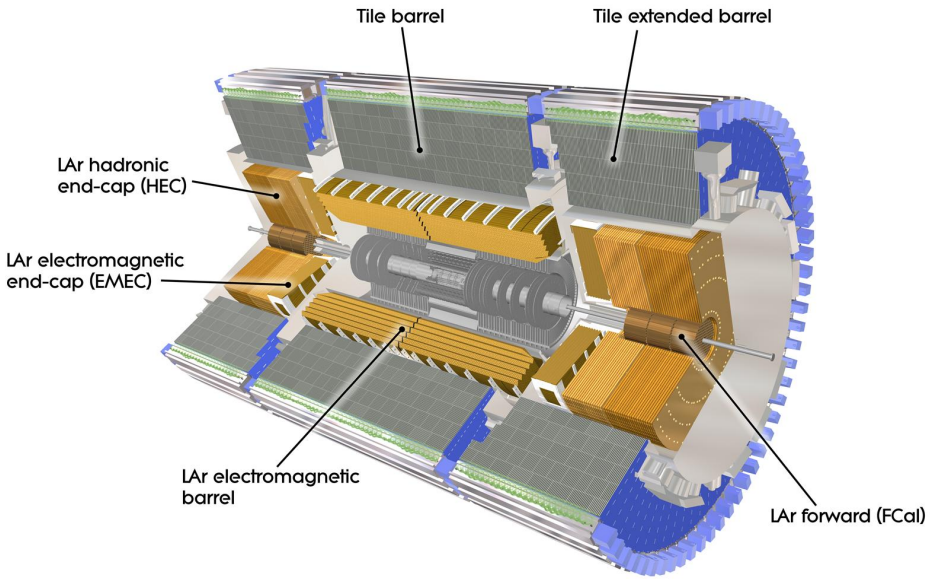

Figure 3.6: View of the ATLAS calorimeter system.

be ionised by the secondary electrons in the narrow gaps. An electric field results in the electrons drifting in the liquid-gaps and being readout by copper electrodes. The charged particles which generate the ionization can be direct products of the hard scatter interaction, the result of conversion (in the case of photons), or from showers originating in the absorbers. The ionization signal is then shaped by electronics which induce a bipolar pulse of integral zero. This shaping is designed to cancel the effect of a constant energy injection into the calorimeter and therefore corrects for the high-luminosity LHC environment and multiple interactions in an average sense.

Hadronic Calorimeter

The hadronic calorimeter is located just behind the EM calorimeter. It measures the hadronic showers that develop from the interactions of the particles with the nuclei of the calorimeters material. Such particles are mainly the result of the hadronization of quark and gluons, or of the hadronic decay of τ leptons.

The energy deposited by hadrons in the hadronic calorimeter varies

much, unlike the electromagnetic showers that have constant shower energy to particle energy ratio. The size of hadronic showers depends linearly on the interaction length λ of the material which is longer than the radiation length.

Detector component	Energy resolution (σ_E/E)	η coverage
EM calorimetry	$10\%/\sqrt{E} \oplus 0.7\%$	± 3.2
Hadronic calorimetry		
Barrel & End-Cap	$50\%/\sqrt{E} \oplus 3\%$	± 3.2
Forward	$100\%/\sqrt{E} \oplus 3.1\%$	± 4.9

Table 3.2: Nominal detector performance limits and coverage for the calorimetric system [1].

Tile Calorimeter

The tile hadronic calorimeter consists of a central barrel section covering the region $|\eta| < 1.0$ and two extended barrel sections for coverage of the region $0.8 < |\eta| < 1.7$. These sections consist of 64 modular wedges. The wedges use 3 mm-thick plastic scintillator tile as the active medium surrounded by approximately 5 mm of steel absorber. Signals are transmitted from the scintillating tiles to photomultiplier tubes (PMTs) via wavelength-shifting fibers. [1] The tile calorimeter has 4,672 read-out channels and a test beam energy resolution for isolated pions of 56% $\text{GeV}^{1/2}$ $/\sqrt{E} \oplus 5.5\%$ at $\eta = 0.35$.

3.2.4 Muon Spectrometer

The Muon Spectrometer is the last sub-detector that a particle may travel through in ATLAS as it is the outermost part of the detector.

The muon system is used for high precision tracking of muons and for triggering on them. For this reason, the magnetic field from the toroid bend the muons, so their momentum and charge can be identified since most tracks in the muon detectors can be considered muons, as few other particles make it to this stage. The detector is composed of two types of muon detectors in three layers. The Monitored Drift Tubes (MDTs) and the Cathode Strip Chambers (CSC). The trajectory is measured using the trigger and high-precision tracking chambers. The main detection instrument are the Monitored Drift Tubes. Each wire in the drift tubes filled with gas is isolated and detects a hit when the gas is ionized by a muon.

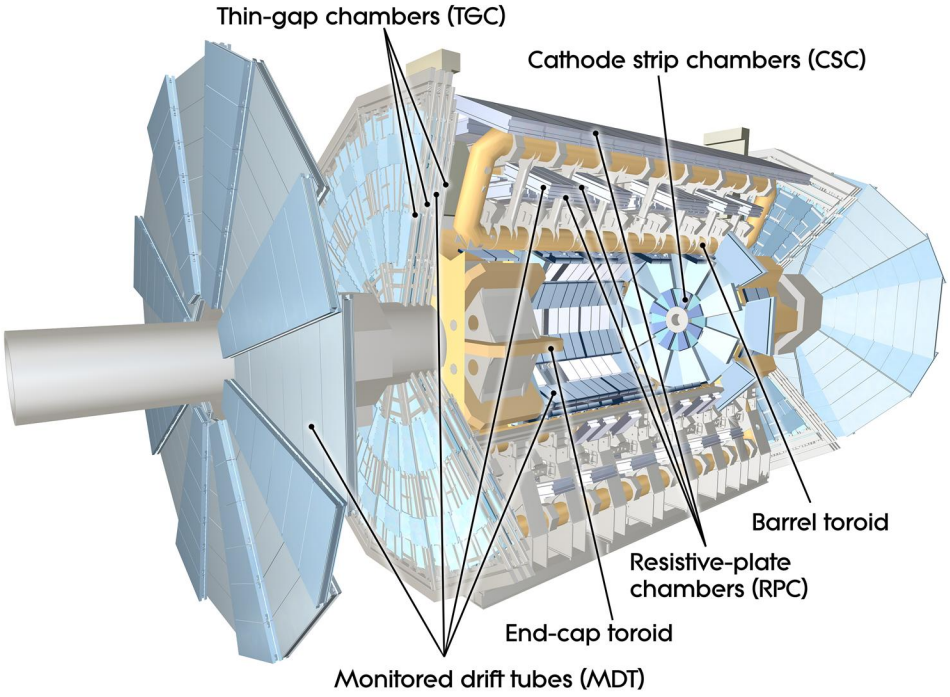

Figure 3.7: Cut-away view of the ATLAS muon system.

The voltage applied between the wire and the tube will move the electrons towards the anode creating large number of charges. The particle's distance from the wire is calculated by measuring the arrival time of the first cluster that passes a certain threshold.

The other technology employed for track detection are CSCs. They are used at large η. The CSCs are constructed from multi-wire proportional chambers filled with an Ar(80%) and CO2(20%) gas mixture [1]. The detection principle is the same as in the MDTs with ionization of the gas creating an avalanche of electrons to the anode wire.

Concerning the triggering function of the muon system, it covers the pseudorapidity range $|\eta| < 2.4$. Resistive Plate Chambers (RPC) are used in the barrel and Thin Gap Chambers (TGC) in the end-cap regions. The trigger chambers provide bunch-crossing identification and measure the muons coordinate in the direction orthogonal to that determined by the MDT and CSC. The efficiency of the muon spectrometer relies heavily on an accurate

mapping of the relative position of the MDT chambers and of the magnetic field. The typical signals left in the ATLAS detector for different particles is drawn in Figure 3.8.

Detector component	Chamber Resolution z/R	Chamber Resolution ϕ
MDT	35 μm in z	N/A
CSC	60 μm in R	5 mm
RPC	10 mm in z	10 mm
TGC	2-6 mm in R	3-7 mm

Table 3.3: Nominal detector performance limits and coverage for the muon system [1].

3.2.5 Forward Detectors

Luminosity measurement using Cerenkov Integrating Detector (LUCID) and Absolute Luminosity For ATLAS (ALFA) are the two detectors measuring the instantaneous luminosity delivered to ATLAS. LUCID is located at 17 m from the interaction point and identifies the relative luminosity through the detection of inelastic pp scattering in the forward direction. ALFA is located further away at 240 m and is as close as 1 mm to the beam [1]. In ALFA the optical theorem connects the elastic-scattering amplitude in the forward direction to the total cross-section and can be used to extract luminosity.

3.2.6 Trigger

At designed luminosity there are over 40 million collisions per second and an event is of the order of one megabyte (MB) in size, it is impossible to record the information about all collision events. Without any filtering the total amount of data from the ATLAS experiment alone would be in sizes of terabytes each second, currently an impossible task. But on the other hand interesting physics occurs mostly at rates of 10, 1 or <0.1 Hz and therefore we are interested in a small fraction of the produced events. The challenge is to quickly identify these events and discard the others. This is done through three levels of trigger: Level-1 (L1), Level-2 (L2) and Event Filter (EF).

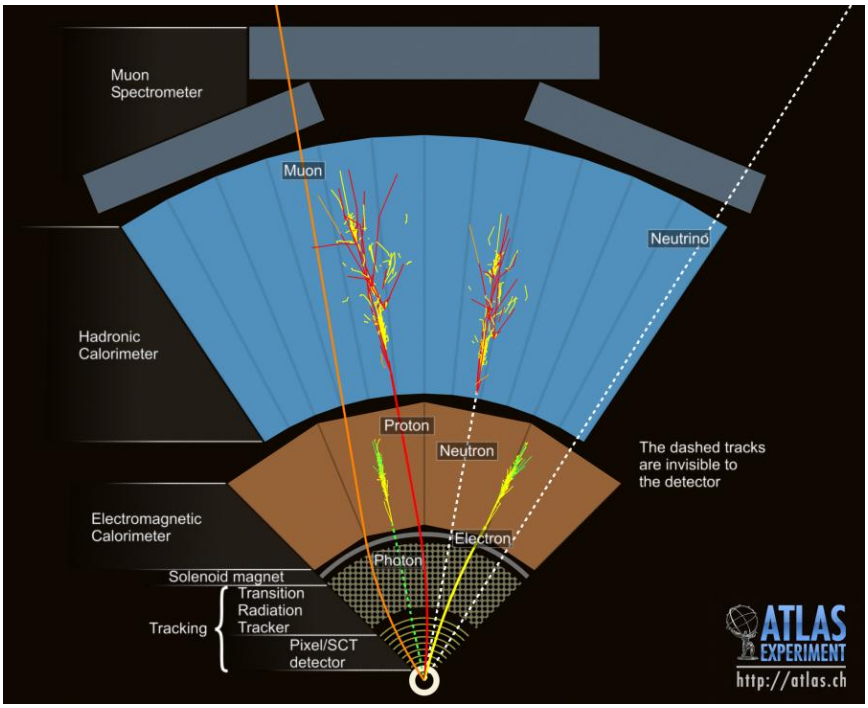

Figure 3.8: The signal from various particles as seen in the ATLAS detector.

The Level-1 Trigger

The L1 is a configurable, pure-hardware trigger designed to make a decision on each event. It operates at the input rate of the bunch-crossing (40 MHz) and reduces it down to 75 kHz. It makes an initial decision based on timing from an electrostatic beam pickup (BPTX), coarse detector information from muon trigger chambers and towers of calorimeter cells, together with multiplicity information from the Minimum Bias Trigger Scintillators (MBTS) and very forward detectors. The maximum time that the L1 has to make a decision is only 2.5 μs from the time of its associated bunch-crossing.

The Level-2 Trigger

L2 triggers make a decision in less than 40 ms and have an output at a rate of 3.5 kHz. It uses the regions of interest (RoIs) identified by the L1 trigger to make a more refined decision. L2 is a software-based trigger which runs more thorough algorithms on the RoIs as there is more time to decide

whether the event in question is interesting [1].

The Event Filter

The final trigger decision is made by the event filter where reconstruction algorithms are run to find particles in the complete detector or just the RoIs. Here EF makes a decision in less than four seconds and gives an output at a rate of 200–400 Hz [1].

3.3 Experimental Signatures

3.3.1 Electrons

Electron reconstruction is first based on the identification of a set of energy clusters in the EM calorimeter where a sliding window algorithm identifies clusters of cells with a size of 3×5 and with at least 2.5 GeV of deposited energy (seed clusters). Both the Inner Detector (ID) and the Electromagnetic (EM) calorimeter are used for electron detection.

In each reconstructed cluster, the reconstruction algorithm looks for a matching track in the ID. An electron should leave a track in the ID. Multiple tracks may be matched to the seed cluster, in this case the one with the smallest distance in ΔR is selected as the best-matched candidate. This requirement is not sufficient in itself to ensure that the signature was caused by an electron. It is very likely that the reconstruction algorithms provide electron candidates which should be accounted as background instead, e.g. converted photons or jets (faking electrons). In order to be able to distinguish between real and fake electrons, there are a number of cuts that are applied on the candidate electron listed here:

- the energy in the Had Calorimeter inside the electron cone,
- the track transverse impact parameter d_0[2],
- the track longitudinal impact parameter z_0[3],
- the shape of the electromagnetic shower,
- the number of hits in the different layers of the ID,

[2] distance in the transverse plane (x, y) between the point of the closest approach of a track to the primary vertex.

[3] z-coordinate of this point.

- the difference between the calorimeter cluster and the extrapolated track positions in η and ϕ,
- and the ratio of the cluster energy to the track momentum.

Three sets of identification criteria are established which define the following electron collections:

- *Loose electrons:* are identified using calorimeter information only. The energy deposition of the electromagnetic shower on the first layer of the hadronic calorimeter (hadronic leakage) is evaluated as well as the shower-shape from the second layer of the EM calorimeter.
- *Medium electrons:* are identified using both calorimeter and tracking information. In addition to selection cuts for "loose" candidates, the first layer of the calorimeter for shower-shape estimates are used along with ID track quality and matching criteria.
  - *medium++:* was created to provide a low energy, high efficiency electron sample which met the trigger bandwidth restrictions for high luminosity[19].
- *Tight electrons:* has the same calorimeter cuts as the "medium" electrons with a tighter requirement for track matching and quality cuts. A number of hits on the Pixel B-Layer and the TRT sub-detectors are also required. In addition, electrons that are matched to converted photons are also rejected.

3.3.2 Muons

Muon reconstruction relies mainly on the muon spectrometer, ID and the calorimeters. The first piece of data used is the existence of a track in the bending plane of a muon station. The tracks are required to be consistent with a particle that is coming from the center of the detector. There needs to be more than one segment candidate that are joined together to reconstruct a muon track. From the curvature of the track the momentum of the muon is calculated. The following identification strategies are used to classify the muon candidates:

- *Standalone muons (SA):* are reconstructed using only MS information. Their track is extrapolated to the beam line for identifying the trajectory and impact parameter.

- *Combined muons (CB):* are formed by combining the calculated tracks from the MS and the ID independently.
- *Segment-tagged (ST) muons:* are ID-reconstructed muons where the track is extrapolated to the MS and then matched with straight-track segments.
- *Calorimeter-tagged (CT) muons:* are ID-reconstructed muons that are extrapolated to the calorimeters.

There are two different algorithms used in ATLAS to reconstruct the muons: STACO, MuId. They both create combined tracks out of pairs of MS-only and ID-only tracks.

- *STACO* uses a statistical combination of the track vectors to obtain the combined track vector,
- *MuId* does a re-fitting in the combined track, starting from the ID track and then adding MS measurements.

3.3.3 Jets

The proton collisions result in large production of quarks and gluons which either come from the hard scattering or from the initial and final state radiation. Subsequently they hadronize into a stream of particles, which can simply be seen as a jet.

Other types of particles e.g. electrons could be misidentified as a jet as well as being identified as an electron. Looking at the η, ϕ distribution of objects can tell us if we are misidentifying them since each object has a unique set of variables.

Jet clustering algorithms are the most important tools in analysing high-energy partons that fragment and emerge as collimated sprays of hadrons.

Jet Algorithms

The mapping from partons to jets is quite complex and it depends mainly on the jet algorithm that is used. In ATLAS and in this analysis the anti-k_T Algorithm [20] has been used. It is a k_T algorithm with negative power in the distance measurement between two objects or between an object and the beam B. The anti-k_T jet algorithm is defined using:

$$d_{ij} = min(k_{Ti}^{2p}, k_{Tj}^{2p}) \frac{\Delta_{ij}^2}{R^2}, \tag{3.5}$$

$$d_{iB} = k_{Ti}^{2p}, \tag{3.6}$$

where $\Delta_{ij}^2 = (y_i - y_j)^2 + (\phi_i - \phi_j)^2$. k_{Ti} is the P_T (transverse momentum) of object i, Δ_{ij} refers to the $\eta - \phi$ distance of two objects i and j, R indicates the jet's size and the parameter p is the power of the energy scale. In practice, d_{ij} is the distance variable between entities (particles, proto-jets) i and j and d_{iB} between entity i and the beam (B).

The algorithm identifies and starts from the smallest of all possible distances d_{ij} between all objects in an event. If d_{ij} is smaller than d_{iB} the objects i and j are combined and their four-momenta are added. Otherwise if $d_{iB} < d_{ij}$, i is considered as a single jet and it is removed from the list of objects. The distances are recalculated and the above procedure is repeated until no entities are left.

The choice of the Δ parameter depends entirely on the analysis, eg. the typical default values used in ATLAS are $\Delta = 0.4$ and $\Delta = 0.6$. For example in top quark pair events a smaller cone size is more suitable, therefore $\Delta = 0.4$ has been chosen.

Jet Calibration

After the clustering of the objects into jets, in order to reconstruct the energy of the jets, they need to be calibrated. Jets are reconstructed using standard topological clusters and calibrated with the local cluster calibration, "LC", which consists of weighting differently the energy deposits arising from EM showers and hadronic showers. MC simulation is used to optimise the corrections applied to the topoclusters. The final jet energy calibration uses the jet energy scale (JES) which corrects the calorimeter response to the true jet energy. It corresponds to the LCW+JES calibration.

3.3.4 Flavor-Tagging

Top quarks decay predominantly into a W boson and a b-quark. Therefore being able to tag the jets that come from b-quarks helps significantly in the $t\bar{t}Z$ signal selection and eventually increases the signal to background ratio. This type of identification is called flavor-tagging or b-tagging if the desired candidates are b-quarks. There are multiple b-tagging algorithms available. For this analysis, an algorithm called MV1 [21] was used.

3.3.5 Missing Transverse Energy - E_T^{miss}

In $t\bar{t}Z$ decays a large part of the event's energy is carried away by the neutrino. We can not directly measure this energy since neutrinos do not leave a trace on any of the detectors components. By using the momentum conservation principle and balancing the contribution of the other objects in the event, it is however possible to reconstruct the energy corresponding to all non-interacting particles in an event. This "missing" energy or momentum, will correspond to the vector sum of the momenta of all non-interacting particles. This is not possible in the longitudinal direction where the exact initial momentum of the interacting partons is not known. Instead, the transverse (x - y) plane is used as it can be assumed that in this direction the partons momentum is zero, hence the missing transverse energy is calculated. E_T^{miss} is then given by:

$$E_T^{miss} = \sqrt{E_x^{miss^2} + E_y^{miss^2}}. \tag{3.7}$$

E_T^{miss}, is calculated from calibrated electrons, muons and jets and the topological clusters falling outside of these objects. The definition used in this analysis is called Egamma10NoTau-RefFinal-STVF, and is defined as:

$$E_{(x,y)}^{miss} = E_{(x,y)}^{e} + E_{(x,y)}^{\gamma} + E_{(x,y)}^{jets} + E_{(x,y)}^{cl} + E_{(x,y)}^{\mu}. \tag{3.8}$$

The electron term ($E_{(x,y)}^{e}$) is calculated using electrons passing the medium++ electron selection and with $E_T > 10$ GeV. The photon term ($E_{(x,y)}^{\gamma}$) is calculated using photons passing the tight electron selection (using Egamma definition) and with $E_T > 10$ GeV. The jet term ($E_{(x,y)}^{jets}$) is calculated using jets with local (x,y) calibration applied, corrected for pileup using the jet vertex fraction, and with $p_T > 20$ GeV [22]. Any remaining topoclusters not associated with electrons, photons or jets with $p_T > 20$ GeV are used to calculate the soft jet term with local calibration. These are combined with remaining low energy calorimeter deposits (with local calibration and energy flow), together with pileup suppression to form the corrected cell out term ($E_{(x,y)}^{cl}$). The muon term ($E_{(x,y)}^{\mu}$) is calculated using all STACO muons passing the selections given in Chapter 4.

Chapter 4

Reconstruction and Selection of $t\bar{t}Z$

4.1 Data and Monte Carlo Samples

The data sample considered for analysis corresponds to a total integrated luminosity of 13.0 fb^{-1}. ATLAS data is divided into runs, which in turn are divided into two-minute sections called luminosity blocks. Each luminosity block is capable of having its own set of data-quality flags. Unstable beams (where much of the detector remains off to protect it from damage), noisy channels, and other detector issues are logged and the affected luminosity blocks are not used for analysis.

Several MC generators are used in this analysis. A brief description of each generator is given below. Fragmentation and hadronisation for the ALPGEN [23] and MC@NLO [24] samples are performed with HERWIG [25], using JIMMY [26] for the underlying event. In case of the MADGRAPH [27] samples, PYTHIA [28] is used for the shower. All MC@NLO, SHERPA and Powheg MC samples are generated using the next-to-leading order PDF set CT10, while the ALPGEN and MADGRAPH samples are generated using the PDF set CTEQ6L1.

PYTHIA and HERWIG: Both of these general purpose generators contain a large number of built-in processes which are generated at the lowest QCD order, therefore they are at fixed leading-order.

ALPGEN: The ALPGEN generator is a leading-order matrix element generator specialized for multi-parton final states. In contrast to PYTHIA and HERWIG, it provides a more accurate description by using perturbation theory on all the relevant tree-level Feynman diagrams with a fixed number of outgoing partons.

JIMMY: It will allow you to generate multiple parton scattering events in hadron-hadron, photon-photon or photon-hadron events.

MADGRAPH: Allows matrix element generation and event generation for any model that can be written as a Lagrangian, using the output of the

FeynRules Feynman rule calculator.

SHERPA: Similarly to ALPGEN it provides a more accurate description of multi-parton final states based on matrix element calculation. However, it can also handle internally the rest of the processes without needing to couple with an external package.

MC@NLO and POWHEG: Primarily used for the production of top quark events. Differences between MC@NLO and POWHEG are due to the treatment of higher orders.

4.2 Selection

The analysis presented in this thesis focuses on $t\bar{t}Z$ events with three leptons in the final state, resulting from decays of type $t\bar{t}(\rightarrow q\bar{q}^{'}b\bar{b}l\nu)Z(\rightarrow ll)$, where l denotes e, μ, or a τ decaying into e or μ.

4.2.1 Object Selection

Electrons

Electrons are identified using the medium++ selection [19], based on information about the shower shape in the EM calorimeter, energy leakage into the hadronic calorimeters and the property of the track and the track-cluster matching. Additional selection cuts are then applied:

- Transverse energy $E_T > 10$ GeV. The electron energy in Monte Carlo is smeared to reproduce the resolution observed in data (as recommended by the EGamma Working Group [29]).
- Cluster pseudorapidity $|\eta^{cl}| < 2.47$.
- Only electrons reconstructed by the egamma-algorithm optimised for high p_T electrons are accepted.
- Electrons which pass regions in the electromagnetic calorimeter where the signal can not be read due to dead optical transmitters or calorimeter problems are discarded.
- An isolation requirement defined as $p_T cone30/E_T$ <0.16 where $p_T cone30$ is the transverse momentum of all other tracks $p_T > 1$ GeV within a cone $\Delta R = \sqrt{(\Delta\eta)^2 + (\Delta\phi)^2} \leq 0.3$ around the electron track and E_T is the electron transverse energy [30].

- An isolation requirement defined as $e_T cone30^{corrected}/E_T < 0.18$, where $e_T cone30^{corrected} = e_T cone30 - A \times N_{vtx}$ and A = 20.15 MeV (17.94 MeV) in data (MC simulation), N_{vtx} is the number of vertices with at least 5 tracks, and $e_T cone30$ is the p_T and energy-density corrected isolation.
- d_0 significance ($|d_0|/\sigma(d_0)$) less than 5.
- $|z_0 \sin\theta|$ less than 0.4 mm.
- The egamma tight++ requirement [19].

Muons

Muons are reconstructed using the STACO (STAtistical COmbination) algorithm combining a reconstructed muon spectrometer track with a matched inner detector track (combined muons) or an inner-detector seeded identification (segment-tagged muons) [31]. Both combined and segment tagged muons are used and the p_T of the MS and ID tracks in MC are smeared before recombining to match the resolution observed in data. Muons of "loose" quality are selected. Additional cuts are then applied:

- Transverse momentum $p_T > 10$ GeV. The muon p_T is shifted and smeared in MC to better reproduce the resolution in data (as recommended by the Muon Combined Performance Group [32][33].
- Pseudorapidity $|\eta| < 2.40$.
- The track must have at least one b-layer hit (if expected).
- The track must have more than 1 pixel hit and at least 6 SCT hits.
- The track must have less than 3 holes in the pixel and SCT.
- The track must satisfy the following TRT requirements:
  - (0.1< $|\eta|$ <1.9): require $n > 5$ and $n_{TRT}^{outliers} < 0.9 \times n$.
  - ($|\eta| < 0.1$ or $|\eta| > 1.9$): if $n > 5$, require $n_{TRT}^{outliers} < 0.9 \times n$.

where $n = n_{TRT}^{hits} + n_{TRT}^{outliers}$.

- An isolation requirement defined as $p_T cone30^{corrected}/p_T$ <0.12, where $p_T cone30^{corrected} = p_T cone30 - A \times N_{vtx}$ and A = 10.98 MeV (6.27 MeV) in data (MC simulation).
- d_0 significance ($|d_0|/\sigma(d_0)$) less than 3.
- $|z_0 \sin\theta|$ less than 1 mm.

Overlap Removal

If two electrons are identified within $\Delta R_{e1,e2} < 0.1$, the lowest energy electron is discarded. Electrons are reconstructed both by the electron and jet reconstruction algorithms. Therefore, if an electron and a jet passing the object selection criteria are closer than $\Delta R = 0.2$, then the electron is kept while the jet is discarded.

Jets may contain leptons from semileptonic b or c decays. While these are in general rejected by the isolation requirement, there still remains a considerable contribution of leptons, mainly muons, which are isolated within a narrow cone of $\Delta R = 0.2$ and at the same time close to the jet axis. After applying the electron-jet overlap removal, all leptons are required to be separated by more than $\Delta R = 0.4$ from the closest jet.

Muons undergoing bremsstrahlung in the detector can often be reconstructed with an overlapping electron that is the result of a misidentified photon. In these cases, both the muon and the electron are badly reconstructed. To reject the above mentioned muons, electrons and muons (after applying electron-jet and lepton-jet overlap removal) found to overlap within $\Delta R = 0.1$ are both discarded.

Jets

Acceptance cuts applied to the jets are:

- $p_T > 20$ GeV
- $|\eta| < 4.5$

After overlap removal, "signal" jets are required to satisfy $p_T > 20$ GeV, $|\eta| < 2.5$, and JVF > 0.5, where JVF is the fraction of the jets track momenta that can be associated with the primary vertex.

Signal jets are classified as b-jet candidates by the MV1 algorithm if the jet $|\eta| < 2.5$ and MV1 > 0.985; this operating point corresponds to an average b-tagging efficiency of $\sim 60\%$ [21].

4.2.2 Trigger Selection

Events in data need to have passed a logical OR of the triggers summarized in Table 4.1. Which triggers can be used depends on the subchannel, eee, eeμ, e$\mu\mu$ and $\mu\mu\mu$. The selection given in the table is the offline threshold ensuring that the signal leptons per event are in the plateau region of the trigger efficiency.

Periods A-E of the 2012 ATLAS collisions data were analysed. The data sample considered for analysis corresponds to a total integrated luminosity of 13.0 fb^{-1}

Trigger	Detail	offline threshold [GeV]
Double e	EF-2e12Tvh-loose1	14,14
	EF-e24vh-medium1-e7-medium1	25,10
Double μ	EF-2mu13	14,14
	EF-mu18-tight-mu8-EFFS	18,8
Combined eμ	EF-e12Tvh-medium1mu8	14,8
	EF-mu18-tight-e7medium1	18, 10

Table 4.1: The triggers used per data period.

Based on the available triggers listed in Table 4.1, events are selected in data. In MC the trigger simulation of Table 4.1 was used.

4.2.3 Event Cleaning

Events are required to satisfy a number of quality cuts:

- Events with jets potentially originating from instrumental effects are rejected. These jets are all "loose bad"[4] jets with $E_T > 20$ GeV and any η, surviving the overlap removal with electrons. This clean up is performed in data and in MC.
- Events with noise bursts and data integrity errors in the LAr calorimeter are removed.
- The leading primary vertex must have five or more tracks.
- Events are discarded if there is a muon surviving overlap removal with a longitudinal impact parameter $|z_0| > 1$ mm or a transverse impact parameter $|d_0| > 0.2$ mm. This selection is designed to suppress potential cosmic background.

4.2.4 Event Selection

The $t\bar{t}Z$ process was produced in two separate samples, one with zero additional parton $t\bar{t}Z$ with a cross section of 67.7 fb and another with one

[4]Bad jets are jets not associated to real energy deposits in the calorimeters, and loose jets refer to 60% b-tagging efficiency.

additional parton $t\bar{t}Zj$ with a cross section of 87.3 fb. The signal MC simulated events must both be combined for analysis with a generated cross section of σ= 155.0 fb at the Leading order with k-factor σ_{NLO}/σ_{LO}= 1.34 [15] [16].

The final state of $t\bar{t}Z$ events used in this analysis is characterised by the presence of three leptons, four jets, two of which originate from b-quarks, and a neutrino escaping the detector.

Selected events are required to have precisely three leptons where two of the leptons are from $Z \to ll$ and the additional lepton is when W in $t \to bW$ decays leptonically ($W \to l\nu$). Furthermore, in order to ensure that the event is consistent with the presence of a semi-leptonic $t\bar{t}$ pair ($t\bar{t} \to b\bar{b}WW \to qq'\, b\bar{b}l\nu$), the event is required to contain four jets with $p_T > 20$ GeV and missing transverse momentum $E_T^{miss} > 25$ GeV corresponding to neutrinos. Additionally at least one pair of leptons with same flavour and opposite-sign charges (SFOS) is required since $Z \to e^+e^-$ or $Z \to \mu^+\mu^-$ [5]. Moreover, at least one such pair is required to satisfy the Z mass window constraint, $|m_{l+l^-} - m_Z| < 10$ GeV, with $m_Z = 91.2$ GeV. In case there are multiple such pairs, the one whose invariant mass is closest to m_Z is taken to contain the lepton pair coming from the Z boson in what follows.

The signal region, denoted SR, requires at least one of the selected jets to be b-tagged by the MV1 algorithm at 60% efficiency.

Figures 4.1–4.8 show various distributions of interest for the signal region. There is good agreement between data and MC.

4.2.5 Optimization

The event selections above were optimised by maximizing the approximate significance Z_N :

$$Z_N = \sqrt{2}\mathrm{erf}^{-1}(1 - 2p) \tag{4.1}$$

where p indicates the p-value. Conservative uncertainties of 30% on the background are included in the Z_N significance where quoted.

[5] In the case of $Z \to \tau^+\tau^-$ we only consider $\tau \to e\nu$ or $\tau \to \mu\nu$. Hadronic decay of τ is not included in the signal region.

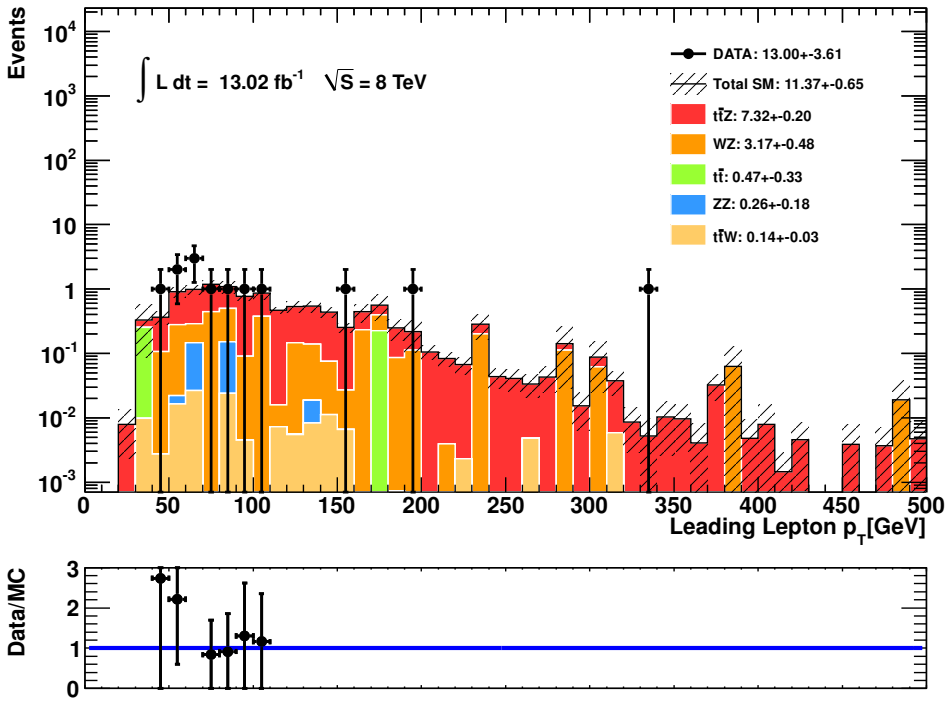

Figure 4.1: SR leading lepton P_T. Errors shown are only statistical.

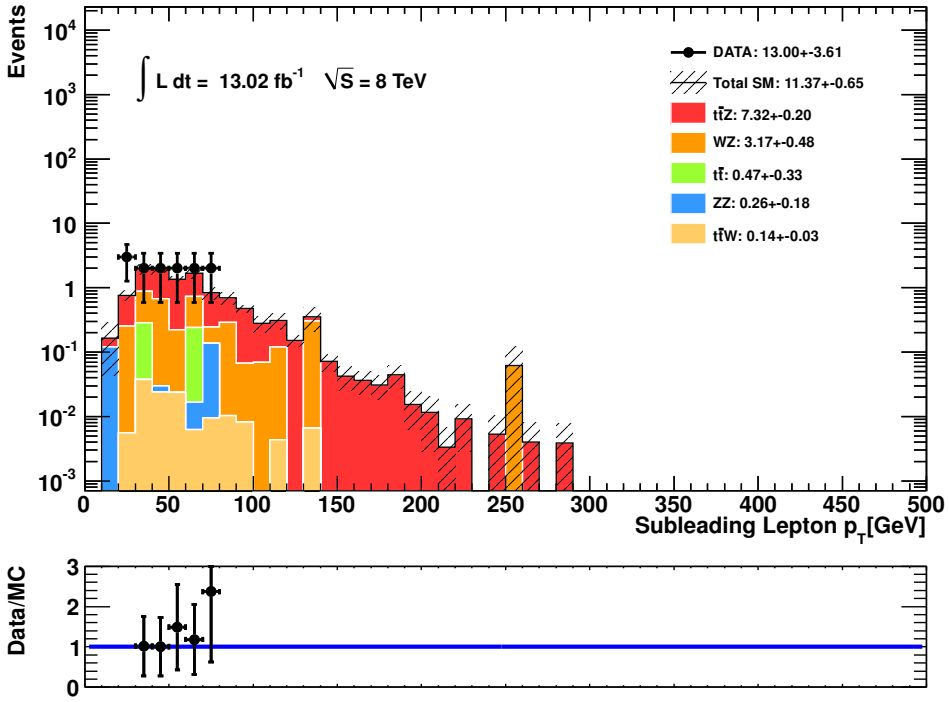

Figure 4.2: SR subLeading lepton P_T. Errors shown are only statistical.

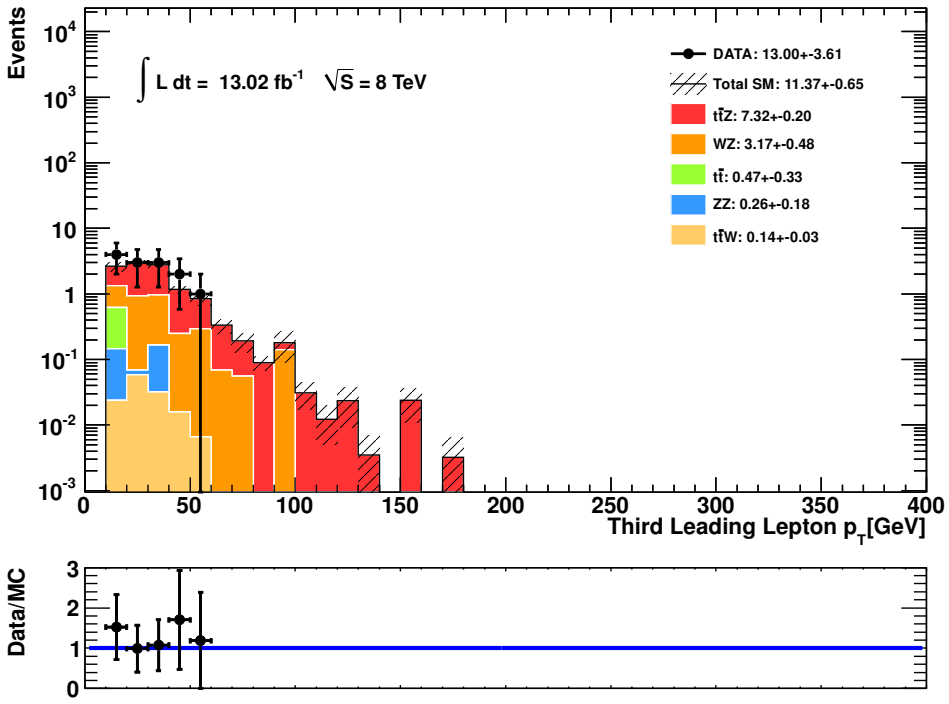

Figure 4.3: SR third leading lepton P_T. Errors shown are only statistical.

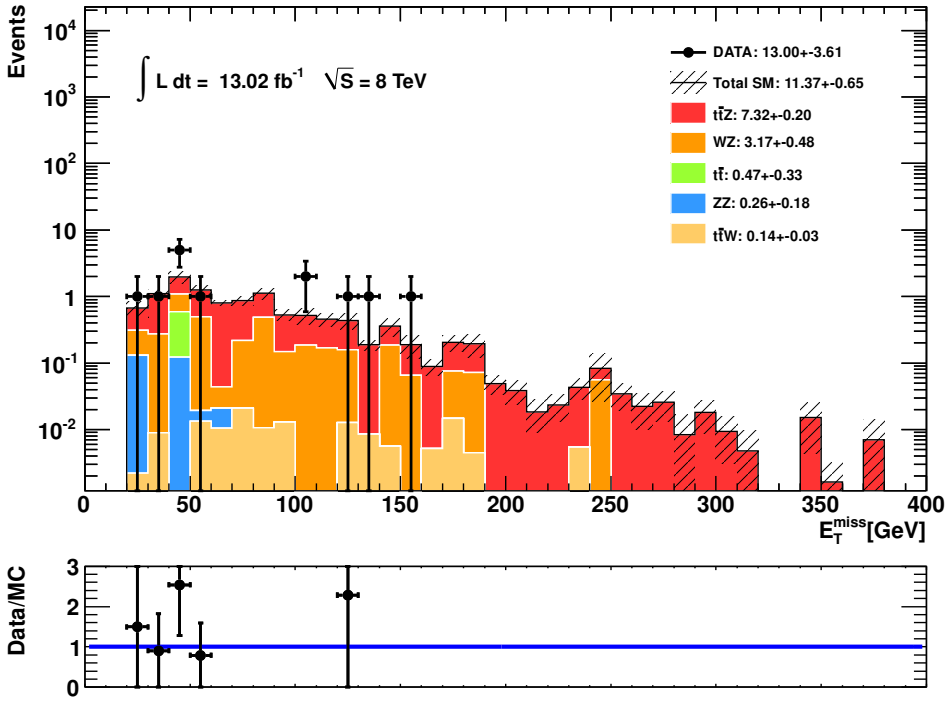

Figure 4.4: SR E_T^{miss}. Errors shown are only statistical.

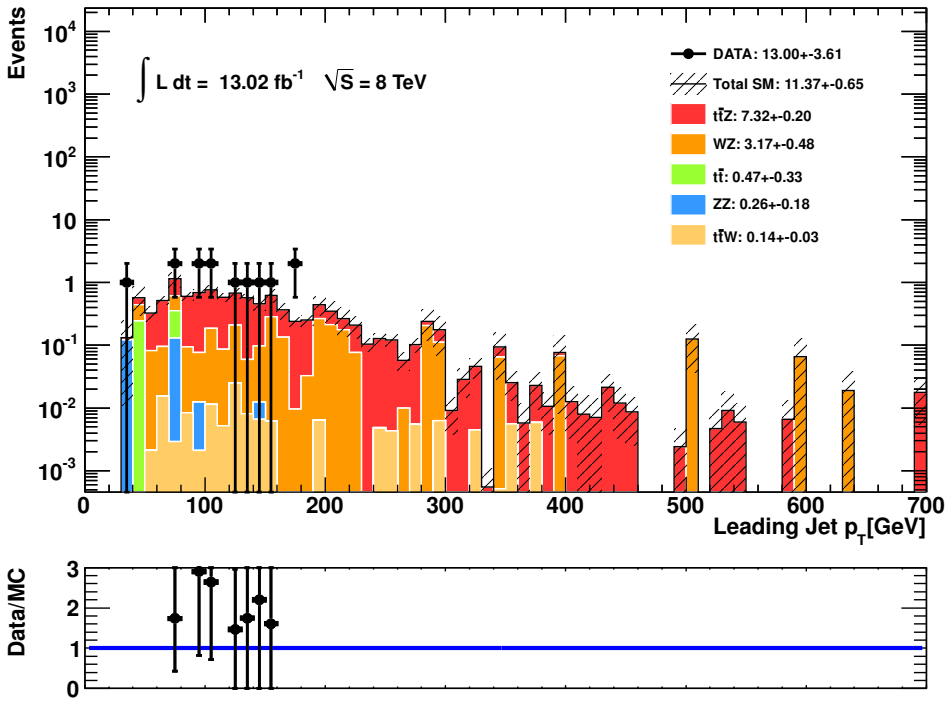

Figure 4.5: SR leading jet P_T. Errors shown are only statistical.

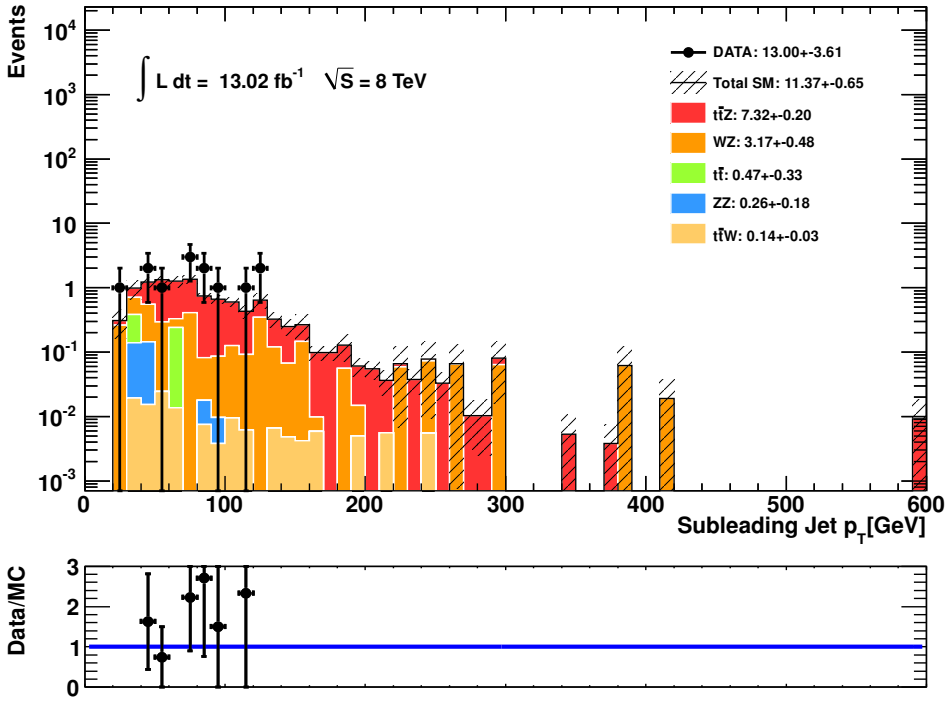

Figure 4.6: SR subleading jet P_T. Errors shown are only statistical.

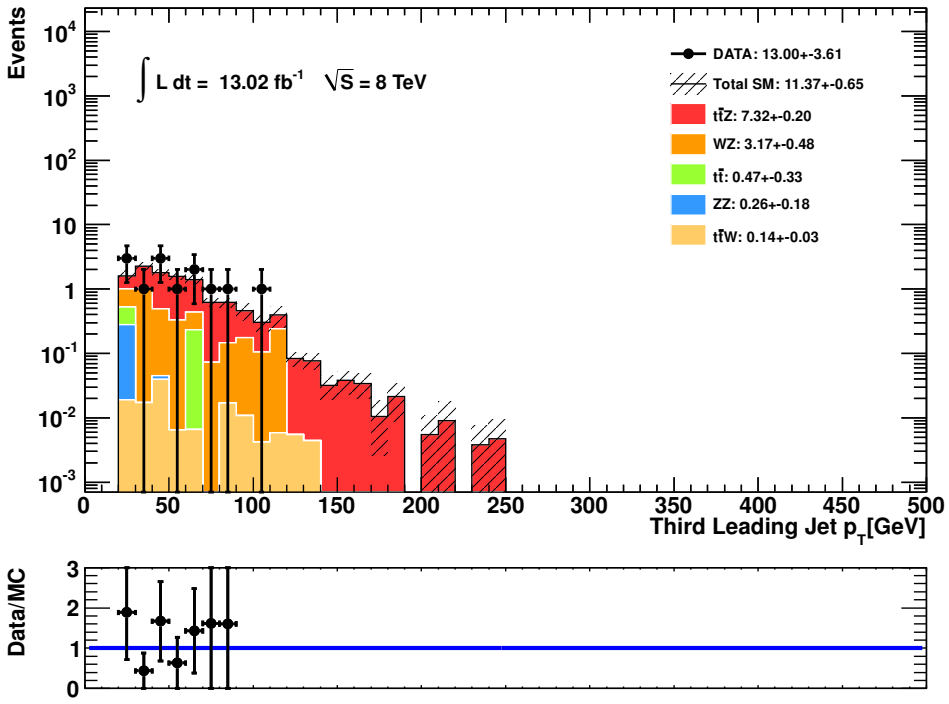

Figure 4.7: SR third leading jet P_T. Errors shown are only statistical.

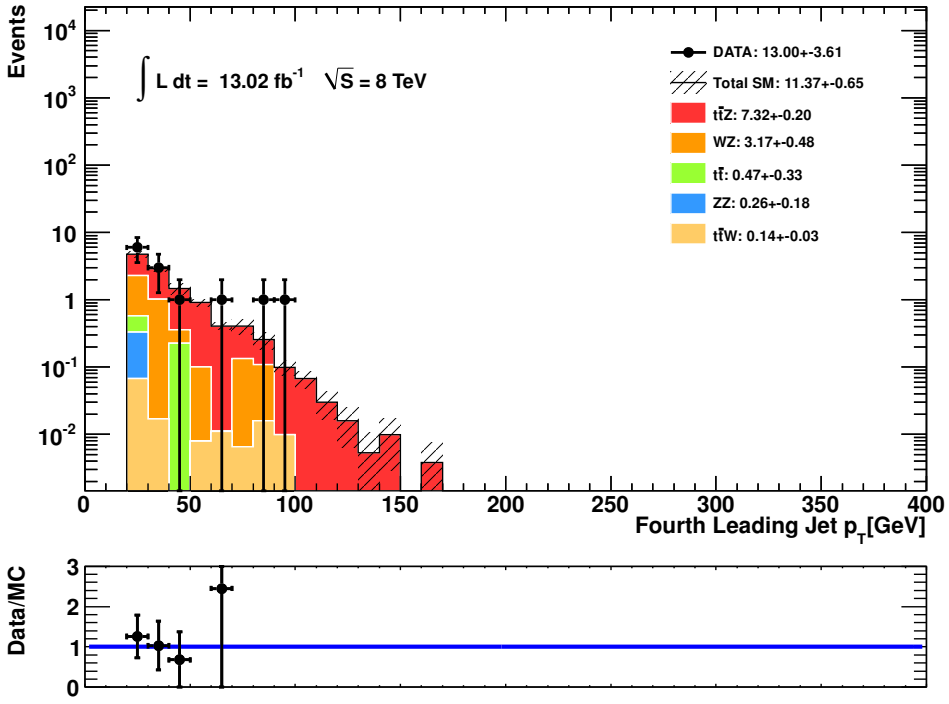

Figure 4.8: SR fourth leading jet P_T. Errors shown are only statistical.

4.3 Backgrounds

Several SM processes can mimic the $t\bar{t}Z$ (MadGraph generator) signal with three leptons and missing transverse energy. The number of signal and background events after each cut is listed in Table 4.4. They are separated into Dibosons, Tops and Boson + jets:

4.3.1 Dibosons

The main diboson backgrounds are WZ and ZZ processes. In the ZZ process we have $ZZ \to llll$ with one undetected lepton or $ZZ \to ll\nu\nu$ with one fake lepton. In the WZ case we have $WZ \to lll\nu$ where a Z decays leptonically and $W \to l\nu$.

The $pp \to llll$, $pp \to lll\nu$ and $pp \to ll\nu\nu$ diboson processes with up to three additional jets were generated with SHERPA. At least two leptons were required to have $p_T > 5$ GeV and $|\eta| < 2.7$ and the minimum invariant mass of same flavor opposite charge leptons was set to 0.2 GeV. Further ZZ/γ^*, WZ/γ^* diboson processes were generated with Powheg for systematics studies. In these samples, leptonic decays are enforced and a filter was applied to select events with a generator level mass of the off-shell Z larger than 0–4 GeV and two leptons with $p_T > 5$ GeV. The results of the cross sections and the corresponding k-factors[6] are presented in Table 4.3.

4.3.2 Top

The $t\bar{t}$ process where $t\bar{t} \to b\bar{b}l\nu l\nu$ with a fake lepton could also be a background to our signal.

The pair-production of top quarks was generated with Powheg and single top production with MC@NLO and AcerMC, using a top quark mass of 172.5 GeV; k-factors are applied to determine the approximate NNLO cross-section when applicable.

4.3.3 Boson + Jets

Z/γ^* + jets processes where $Z/\gamma^* \to ll$ + jets with a fake lepton are also potential background to the $t\bar{t}Z$ signal.

Samples of W and Z/γ^* production in association with up to five light/heavy jets are produced with Sherpa. In this case, heavy jets refers to b and c quarks.

[6] σ_{NLO}/σ_{LO}

Process	σ [pb]	k-factor	filter efficiency
ZZ (4e) Powheg	0.08	1	0.91
ZZ (2e2μ) Powheg	0.18	1	0.83
ZZ (2e2τ) Powheg	0.18	1	0.58
ZZ (4μ) Powheg	0.08	1	0.91
ZZ (2μ2τ) Powheg	0.18	1	0.59
ZZ (4τ) Powheg	0.08	1	0.11
WZ ($e^-\bar{\nu_e}e^+e^-$) Powheg	1.41	1	0.29
WZ ($e^-\bar{\nu_e}\mu^+\mu^-$) Powheg	0.94	1	0.35
WZ ($e^-\bar{\nu_e}\tau^+\tau^-$) Powheg	0.17	1	0.17
WZ ($\mu^-\bar{\nu_\mu}e^+e^-$) Powheg	1.40	1	0.29
WZ ($\mu^-\bar{\nu_\mu}\mu^+\mu^-$) Powheg	0.95	1	0.35
WZ ($\mu^-\bar{\nu_\mu}\tau^+\tau^-$) Powheg	0.17	1	0.17
WZ ($\tau^-\bar{\nu_\tau}e^+e^-$) Powheg	1.40	1	0.14
WZ ($\tau^-\bar{\nu_\tau}\mu^+\mu^-$) Powheg	0.94	1	0.18
WZ ($\tau^-\bar{\nu_\tau}\tau^+\tau^-$) Powheg	0.17	1	0.06
WZ ($e^+\nu_e e^+e^-$) Powheg	0.98	1	0.30
WZ ($e^+\nu_e\mu^+\mu^-$) Powheg	0.64	1	0.35
WZ ($e^+\nu_e\tau^+\tau^-$) Powheg	0.11	1	0.16
WZ ($\mu^+\nu_\mu e^+e^-$) Powheg	0.94	1	0.30
WZ ($\mu^+\nu_\mu\mu^+\mu^-$) Powheg	0.65	1	0.35
WZ ($\mu^+\nu_\mu\tau^+\tau^-$) Powheg	0.11	1	0.16
WZ ($\mu^+\nu_\tau e^+e^-$) Powheg	0.94	1	0.15
WZ ($\tau^+\nu_\tau\mu^+\mu^-$) Powheg	0.64	1	0.19
WZ ($\tau^+\nu_\tau\tau^+\tau^-$) Powheg	0.11	1	0.06

Table 4.2: Samples used for systematics studies. Filters include lepton number, p_T, and η cuts to reduce computation time.

Process	σ [pb]	k-factor	filter efficiency
ZZ (4l) Sherpa	8.74	1.11	1
ZW (3l) Sherpa	9.75	1.06	1
ZZ (2l2ν) Sherpa	0.50	1.14	1
WW (2l2ν) Sherpa	5.50	1.07	1
W$\gamma(e\nu)$ Sherpa	163.11	1	1
W $\gamma(\mu\nu)$ Sherpa	162.74	1	1
W $\gamma(\tau\nu)$ Sherpa	162.00	1	1
Z$\gamma(ee)$ Sherpa	32.26	1	1
Z$\gamma(\mu\mu)$ Sherpa	32.32	1	1
Z$\gamma(\tau\tau)$ Sherpa	32.33	1	1
$t\bar{t}W$ MadGraph	0.10	1.18	1
$t\bar{t}W + jet$ MadGraph	0.09	1.18	1
$t\bar{t}WW$ MadGraph	9.19 $\times 10^{-4}$	1.34	1
tt not all-hadronic Powheg	238.06	1	0.54
Wt MC@NLO	20.66	1.08	1
t-channel $e\nu$ AcerMC	8.60	1.10	1
t-channel $\mu\nu$ AcerMC	8.60	1.1	1
t-channel $\tau\nu$ AcerMC	8.60	1.1	1
s-channel $e\nu$ MC@NLO	0.56	1.07	1
s-channel $\mu\nu$ MC@NLO	0.56	1.07	1
s-channel $\tau\nu$ MC@NLO	0.56	1.07	1
Z $\rightarrow e^+e^-$ Sherpa	1207.90	1	1
Z $\rightarrow \mu^+\mu^-$ Sherpa	1207.80	1	1
Z $\rightarrow \tau^+\tau^-$ Sherpa	1207.10	1	1
W $\rightarrow e\nu$ Sherpa	11878.00	1	1
W $\rightarrow \mu\nu$ Sherpa	11879.00	1	1
W $\rightarrow \tau\nu$ Sherpa	11872.00	1	1

Table 4.3: The background MC samples used for this analyses. Filters include lepton number, p_T, and η cuts to reduce computation time.

Selection	==3l	SFOS	$> 4j$	$E_T^{miss} > 25$ GeV	jets $p_T > 20$ $p_T^1 > 30$ GeV	$\lvert m_{l^+l^-} - m_Z \rvert < 10$ GeV
$t\bar{t} + Z$	23.0 ± 0.4	22.3 ± 0.3	12.5 ± 0.3	11.2 ± 0.3	11.2 ± 0.3	10.2 ± 0.2
$t\bar{t} + W$	10.91 ± 0.25	8.09 ± 0.22	1.44 ± 0.09	1.34 ± 0.09	1.34 ± 0.09	0.19 ± 0.03
ZZ	1028.15 ±10.56	1023.62 ± 10.54	7.76 ± 0.97	4.73 ± 0.77	4.73 ± 0.77	2.43 ± 0.53
WZ	1545.30 ± 10.96	1535.82 ± 10.93	32.81 ± 1.59	27.88 ± 1.46	27.48 ± 1.45	22.02 ± 1.29
$t\bar{t}$	160.33 ± 5.43	120.64± 4.71	15.80 ± 1.73	13.91 ± 1.61	13.91 ± 1.61	2.13 ± 0.69
t	10.92 ± 1.70	7.29 ± 1.35	0.55 ± 0.39	0.31 ± 0.31	0.31 ± 0.31	0
WW	4.00 ± 0.40	3.34± 0.37	0.02 ± 0.02	0.02 ± 0.02	0.02 ± 0.02	0
$Z + jets$	2364.20 ± 102.74	2357.28± 102.66	17.82 ± 5.93	6.21 ± 2.92	6.21 ± 2.92	5.19 ± 2.80
Background	5123.99 ± 104.02	5056.20 ± 103.89	76.26 ± 7.61	54.44 ± 3.73	54.04 ± 3.73	31.96 ± 3.20
MC Total	5146.99 ± 104.0	5078.5 ± 103.9	88.76 ± 7.61	65.64 ± 3.74	65.24 ± 3.74	42.16 ± 3.21
Data	4899.00 ± 69.99	4818.00 ± 69.41	92.70 ± 7.1	71.00 ± 8.43	71.00 ± 8.43	45.00 ± 6.71
Z_N	0.014	0.013	0.44	0.51	0.53	0.74

Selection	select b	$p_T^3 > 15$ GeV
$t\bar{t} + Z$	8.1 ± 0.2	7.3 ± 0.2
$t\bar{t} + W$	0.16 ± 0.03	0.14 ± 0.03
ZZ	0.33 ± 0.19	0.26 ± 0.18
WZ	3.43 ± 0.50	3.17 ± 0.48
$t\bar{t}$	1.16 ± 0.51	0.47 ± 0.33
$Z + jets$	0.48 ± 0.48	0
Background	5.57 ± 0.89	4.05 ± 0.62
MC Total	13.67 ± 0.91	11.37 ± 0.65
Data	15.00 ± 3.87	13.00 ± 3.61
Z_N	2.11	2.32

Table 4.4: Cut C0 includes cosmic veto, dilepton trigger and jet/lepton quality requirements. Only events with three leptons in the final state, resulting from decays of type $t\bar{t}(\rightarrow q\bar{q}^{'}b\bar{b}l\nu)Z(\ \rightarrow\ ll)$, where l denotes e, μ, or a τ decaying into e or μ are considered. Errors shown are only statistical.

4.4 Control Regions

To validate the background modelling, the total background is estimated in dedicated Control regions and the obtained results are compared to the observed data. Since very few events in data and simulation pass the full event selection, it is useful to consider control regions with somewhat looser cuts to verify that the SM background processes that may have three real leptons in the final state are correctly modelled by simulation.

4.4.1 WZ + Jets Control Region

Control regions CRk (with k = 3, 4) require events to contain three leptons, two of which must form an SFOS pair. At least one such pair is required to satisfy the Z mass window constrain, E_T^{miss} >25 GeV, and exactly k jets with p_T >20 GeV. On the other hand, the SR requires one of the jets to be b-tagged and selects events with four or more jets. These control regions are dominated by the WZ + jets process. Figures 4.9–4.18 show various distributions of interest for control regions CR3, CR4. There is good agreement between data and MC

4.4.2 Z + Jets Control Region

Z + jets events with a fake lepton are expected to have low missing transverse energy . Therefore two Z + jets control regions called ZCR1/2 are considered similar to the WZ + jets control regions without requiring any missing transverse energy cut . The jet requirements are also dropped for the Z + jets control region, in order to enhance statistics. In addition, 1 b-tagged jets may be required, corresponding to control regions ZCR2. Figures 4.19–4.30 show various distributions of interest for control regions ZCR1, ZCR2. There is good agreement between data and MC.

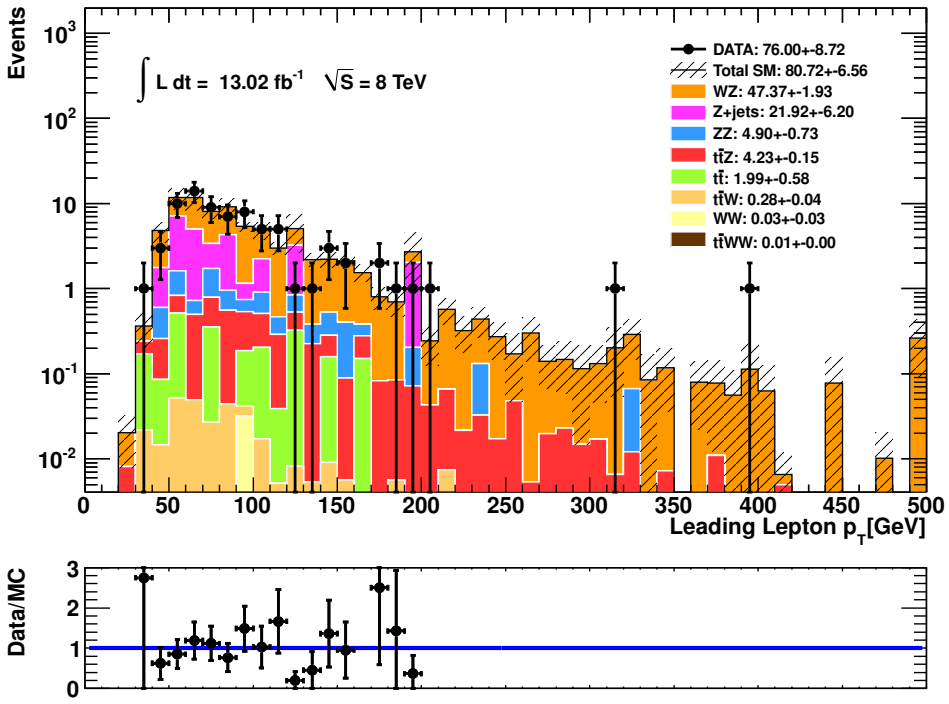

Figure 4.9: CR3 leading lepton P_T. Errors shown are only statistical.

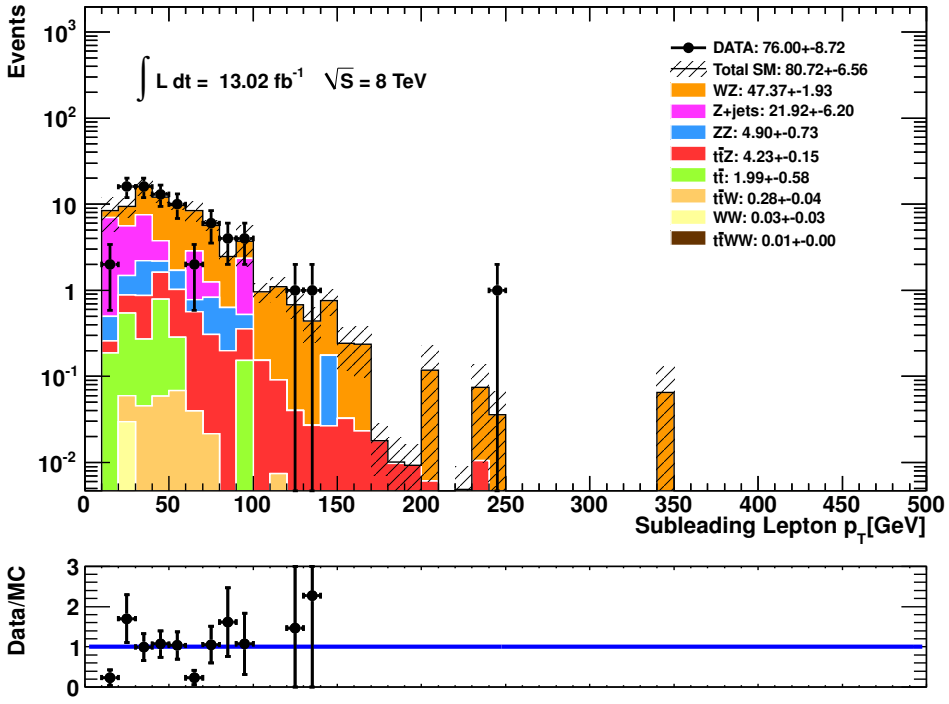

Figure 4.10: CR3 lepton P_T^2. Errors shown are only statistical.

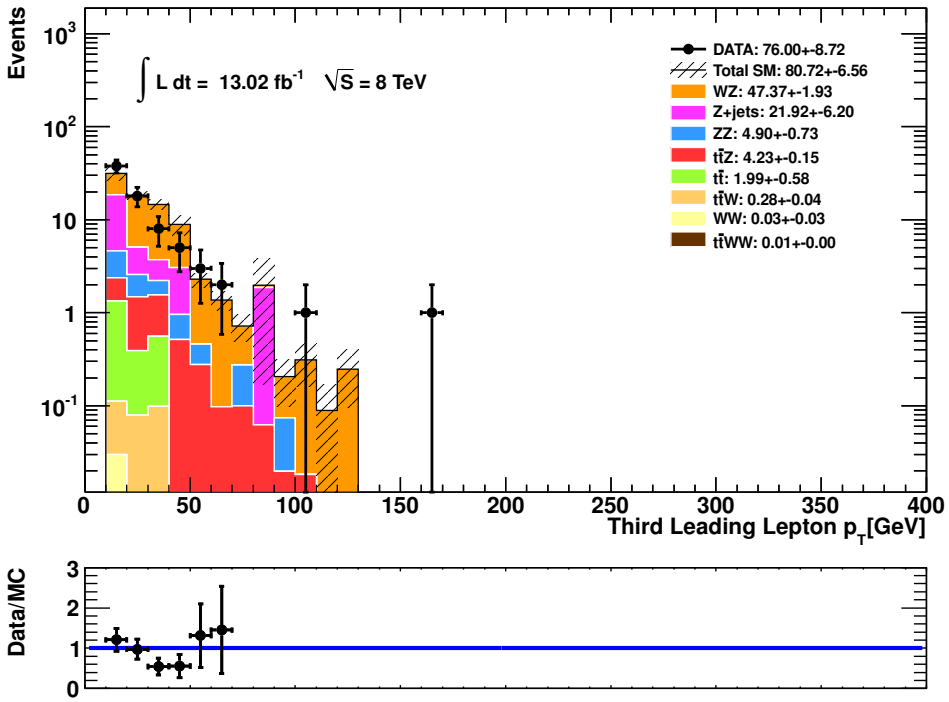

Figure 4.11: CR3 lepton P_T^3. Errors shown are only statistical.

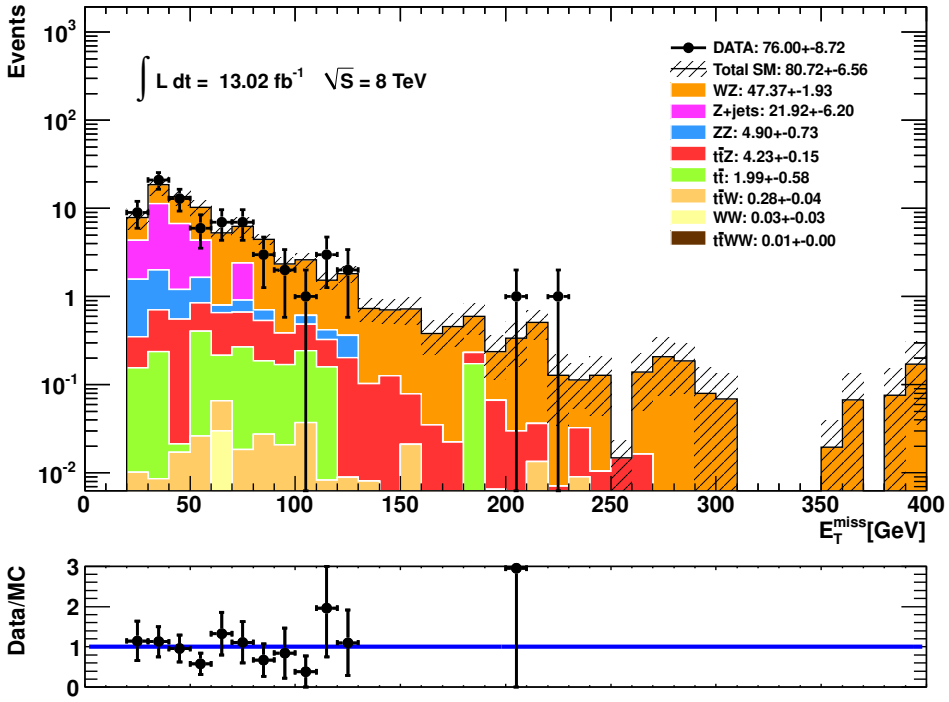

Figure 4.12: CR3 E_T^{miss}. Errors shown are only statistical.

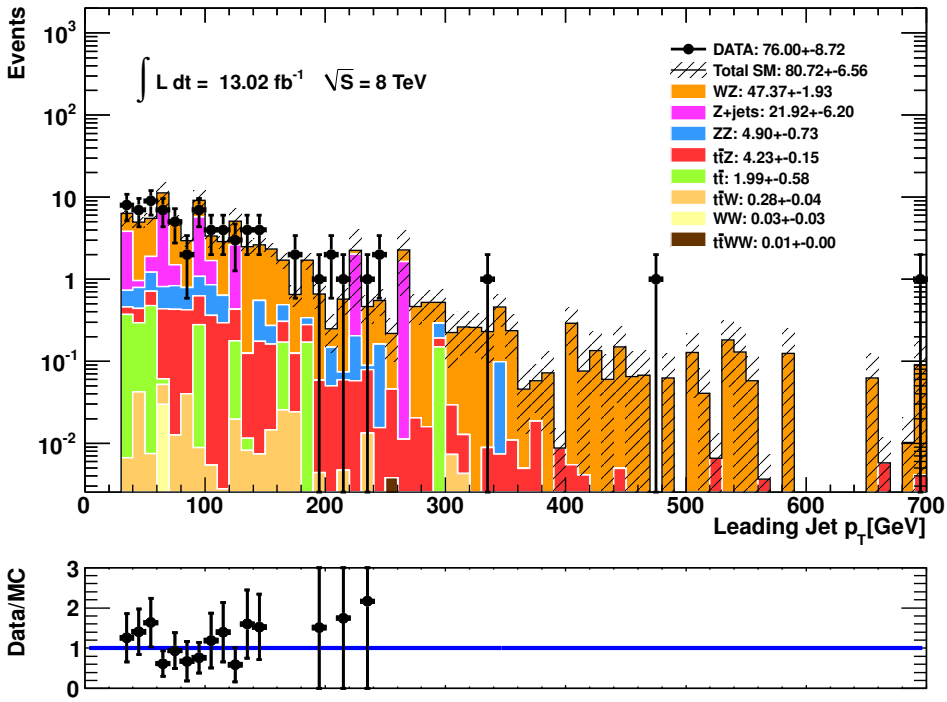

Figure 4.13: CR3 leading jet P_T. Errors shown are only statistical.

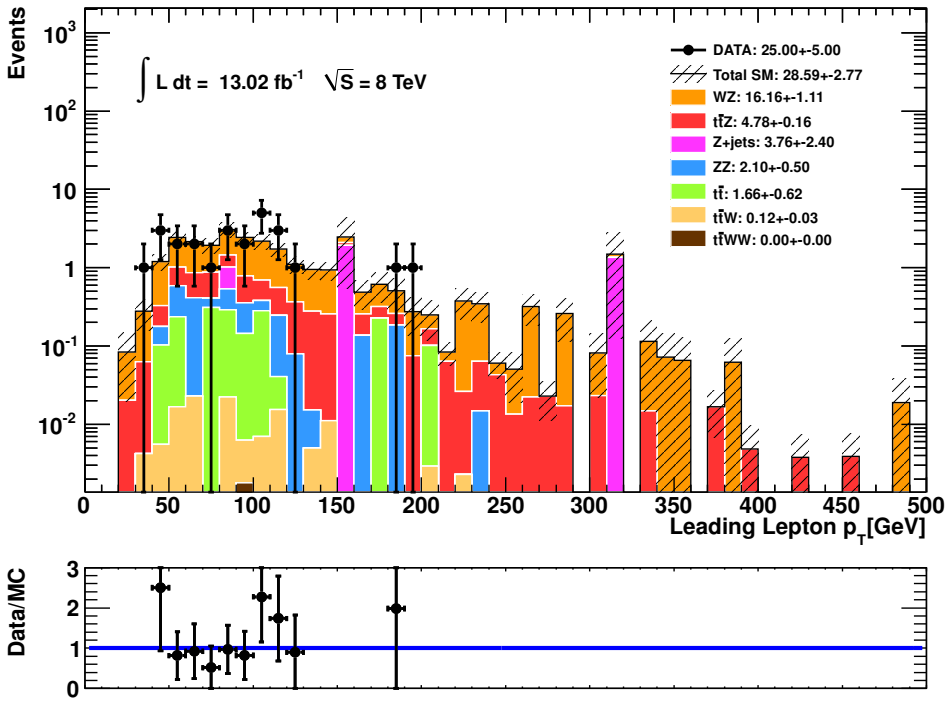

Figure 4.14: CR4 leading lepton P_T. Errors shown are only statistical.

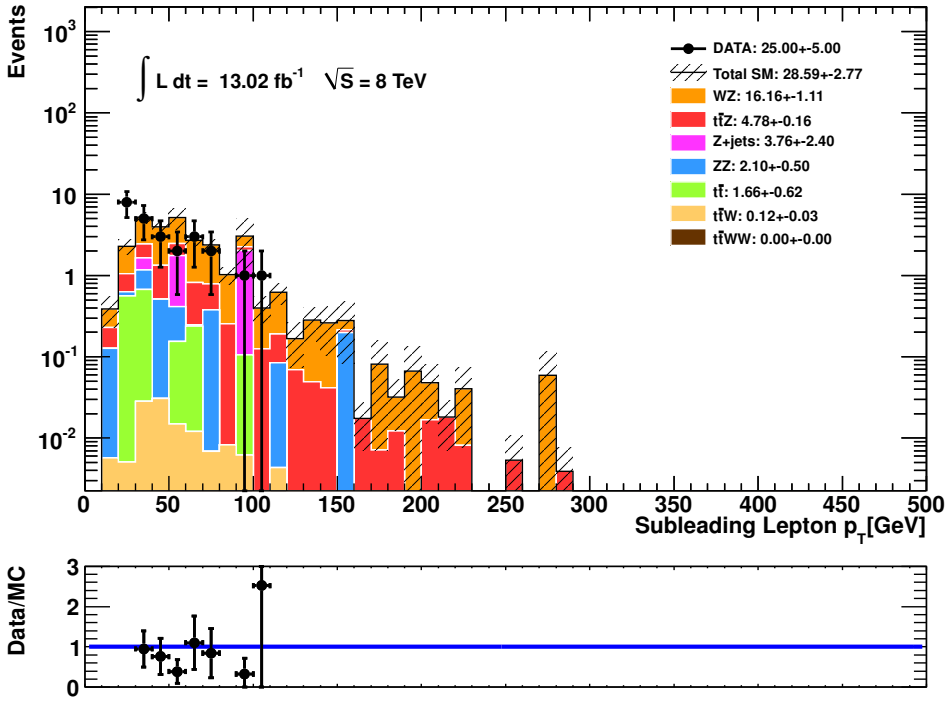

Figure 4.15: CR4 lepton P_T^2. Errors shown are only statistical.

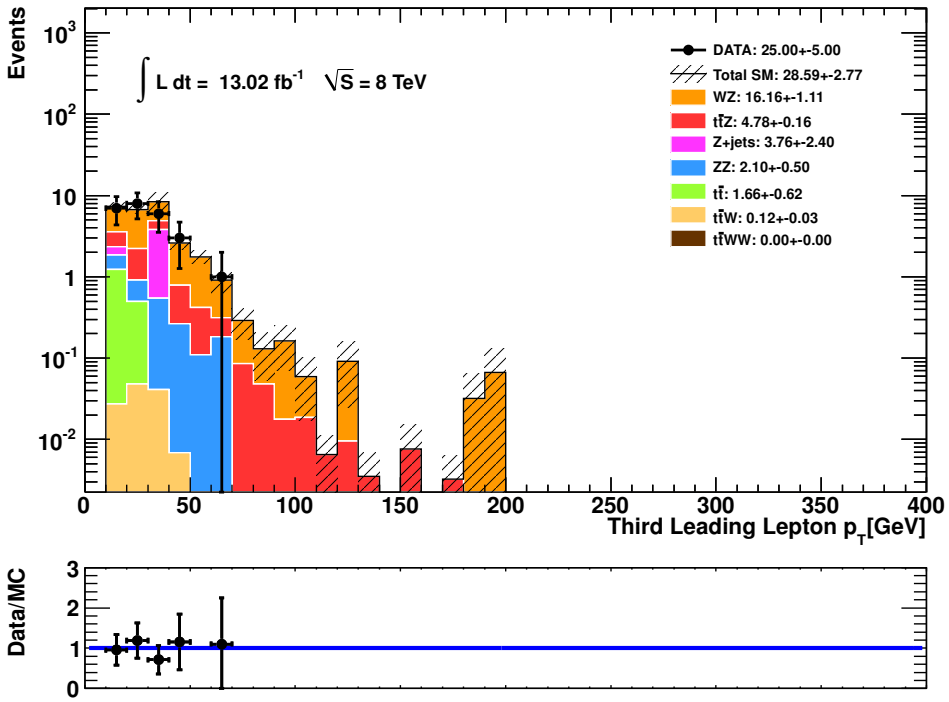

Figure 4.16: CR4 lepton P_T^3. Errors shown are only statistical.

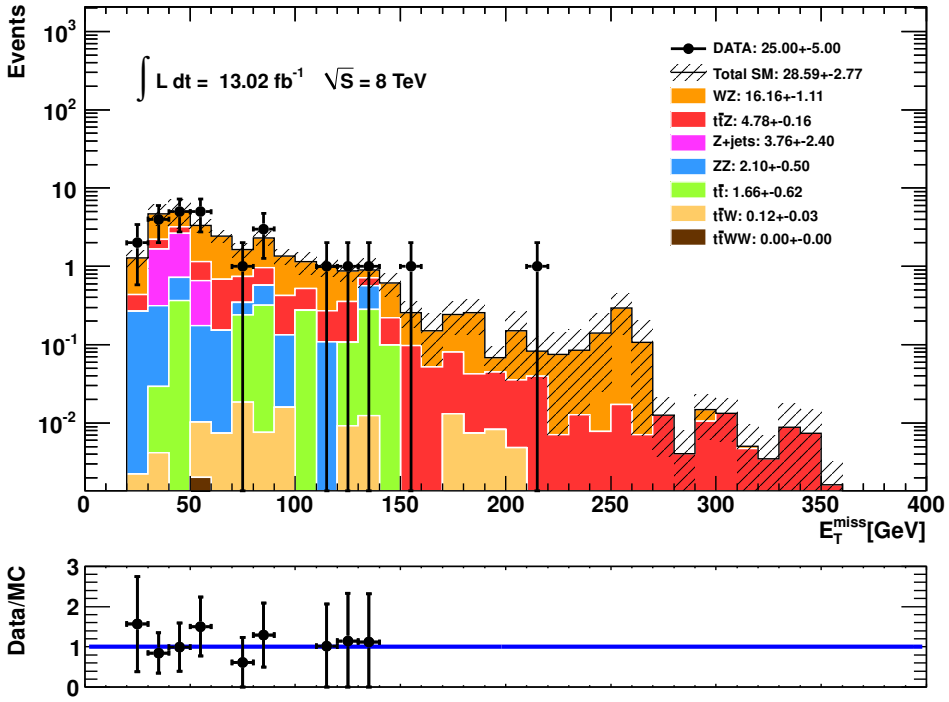

Figure 4.17: CR4 E_T^{miss}. Errors shown are only statistical.

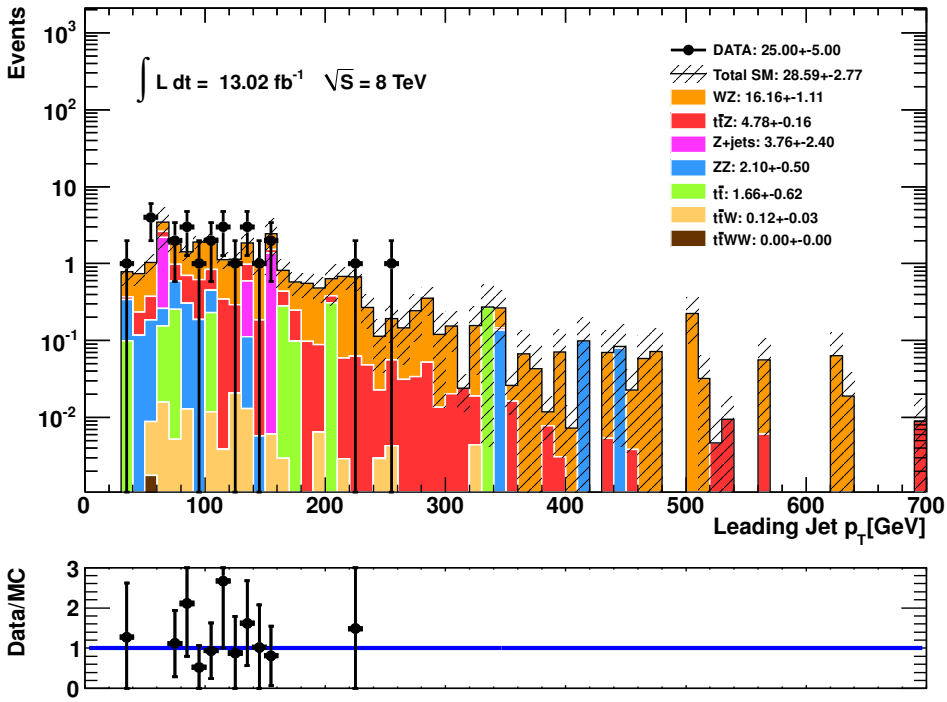

Figure 4.18: CR4 leading jet P_T. Errors shown are only statistical.

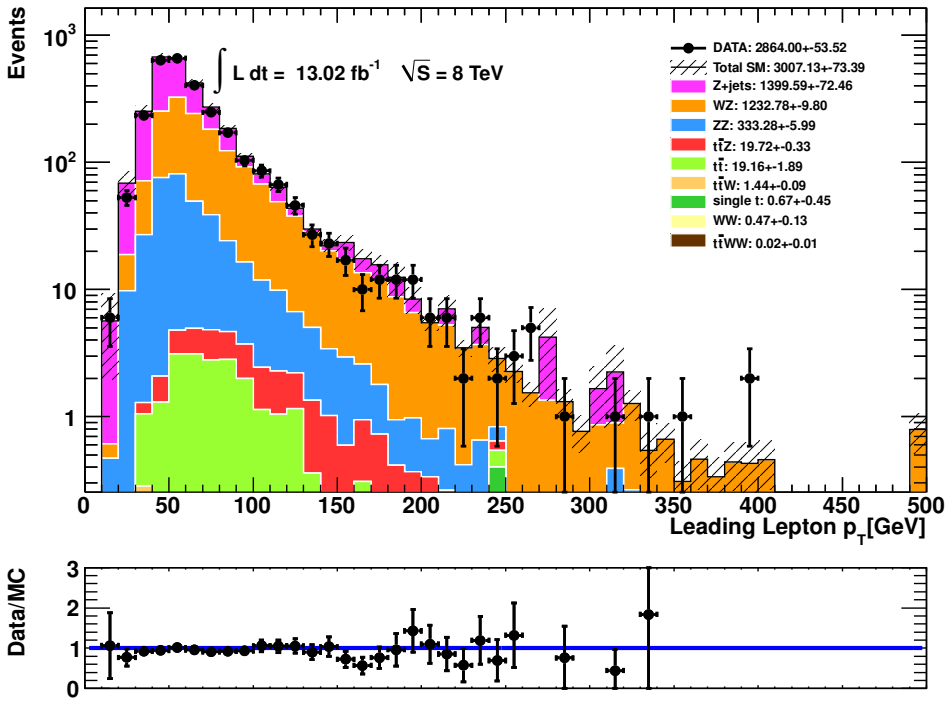

Figure 4.19: ZCR1 leading lepton P_T. Errors shown are only statistical.

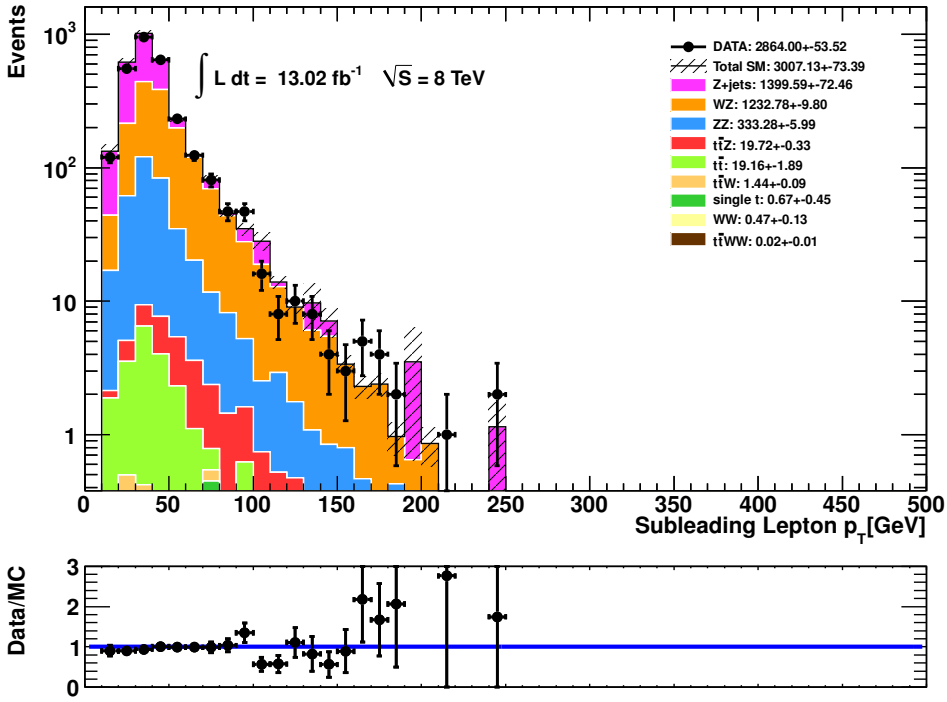

Figure 4.20: ZCR1 lepton P_T^2. Errors shown are only statistical.

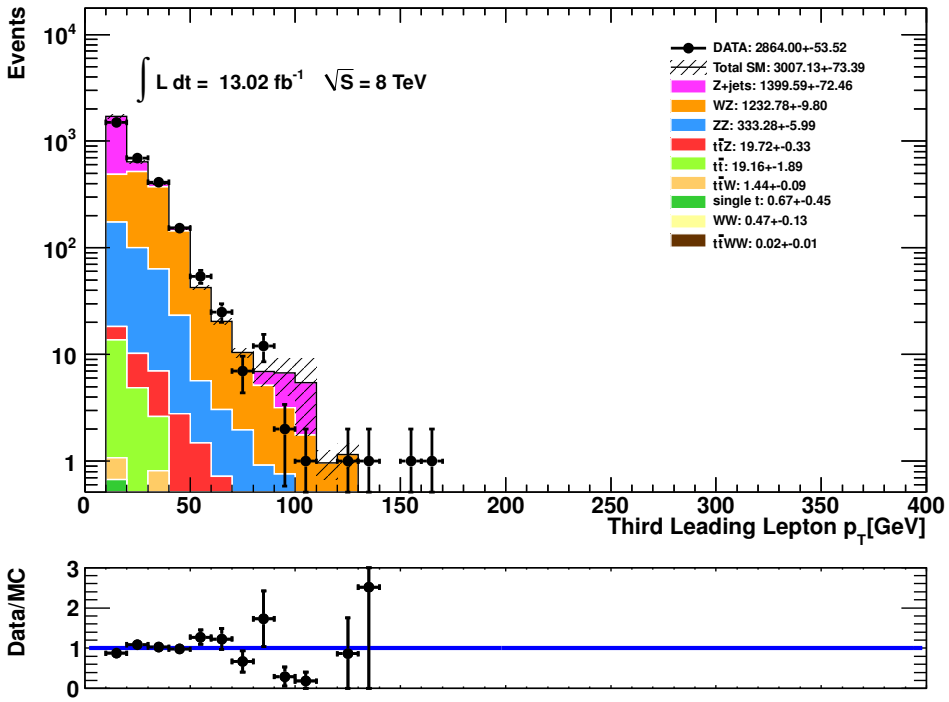

Figure 4.21: ZCR1 lepton P_T^3. Errors shown are only statistical.

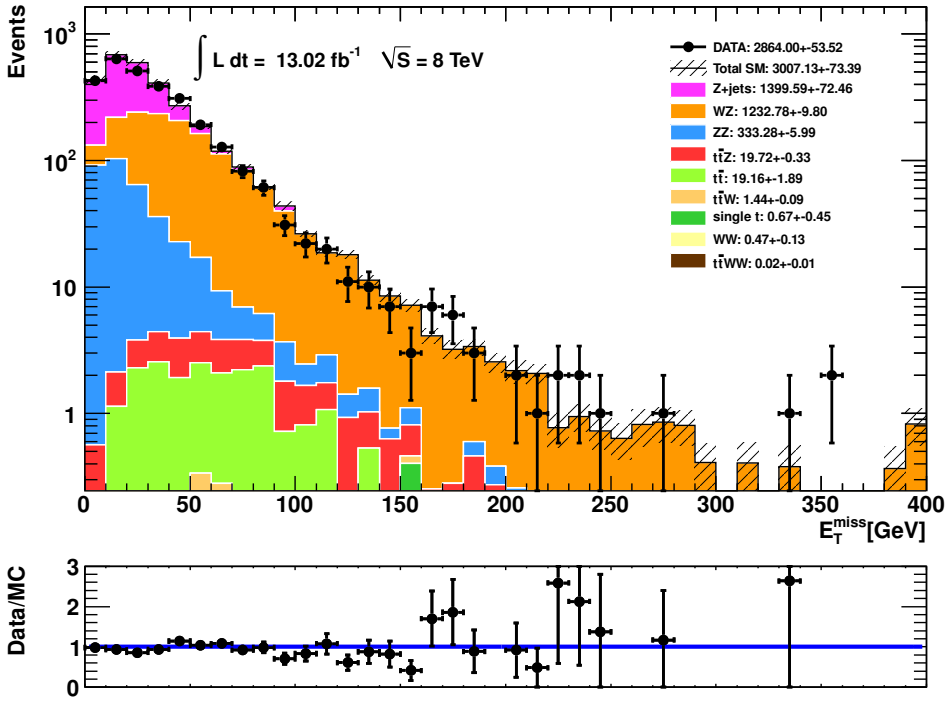

Figure 4.22: ZCR1 E_T^{miss}. Errors shown are only statistical.

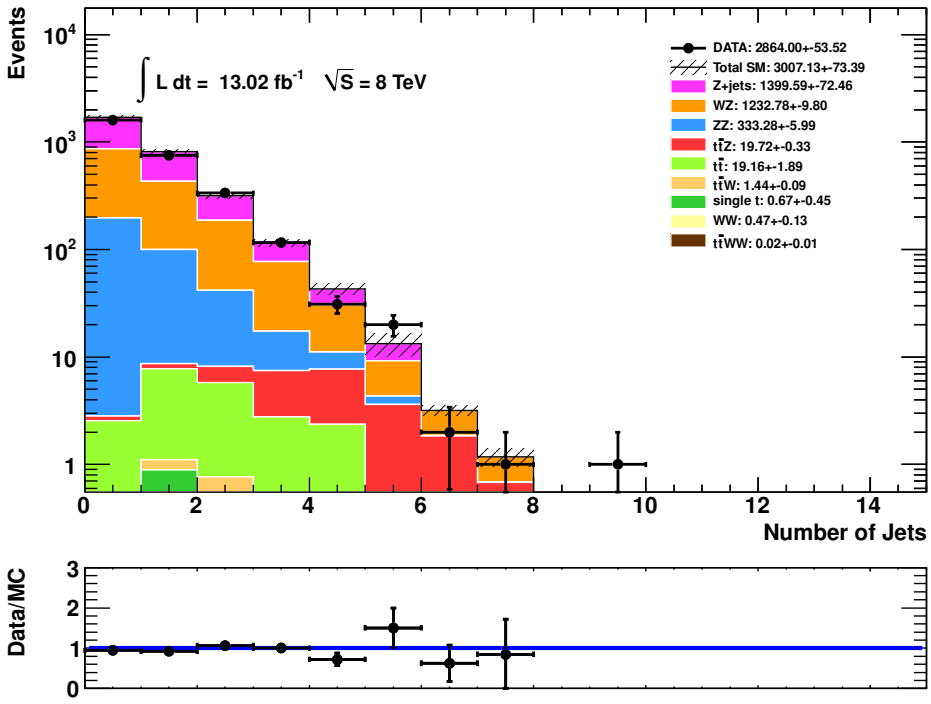

Figure 4.23: ZCR1 number of jets. Errors shown are only statistical.

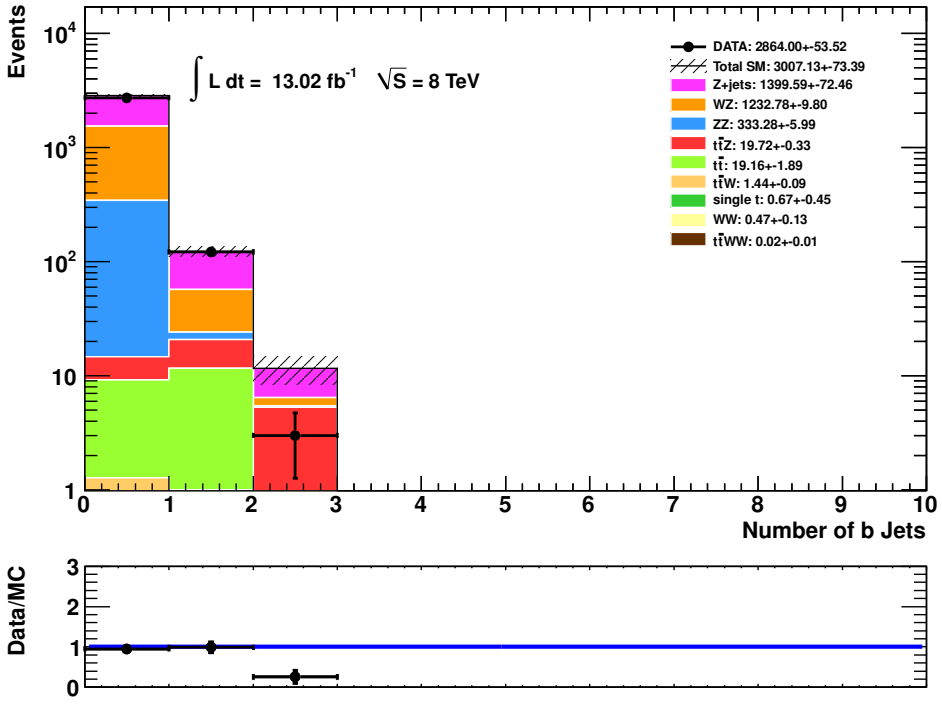

Figure 4.24: ZCR1 number of b jets. Errors shown are only statistical.

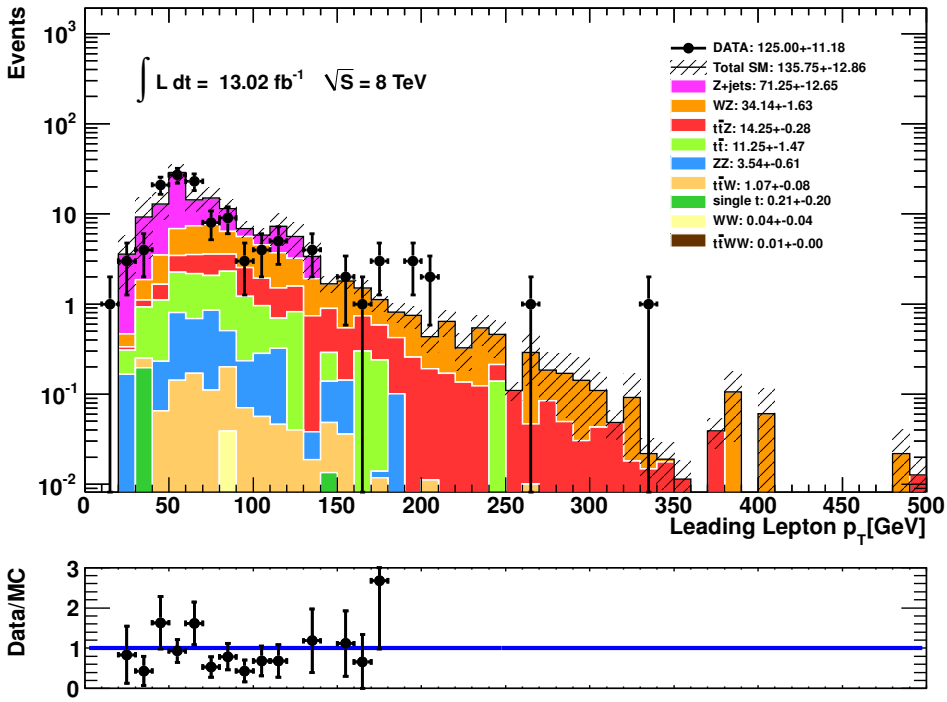

Figure 4.25: ZCR2 leading lepton P_T. Errors shown are only statistical.

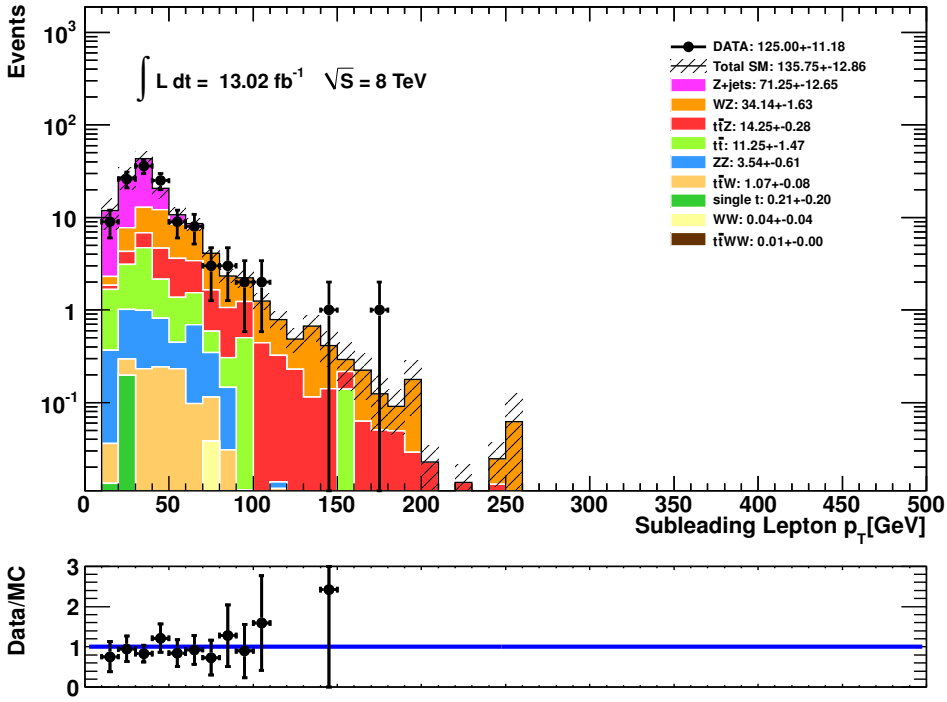

Figure 4.26: ZCR2 lepton P_T^2. Errors shown are only statistical.

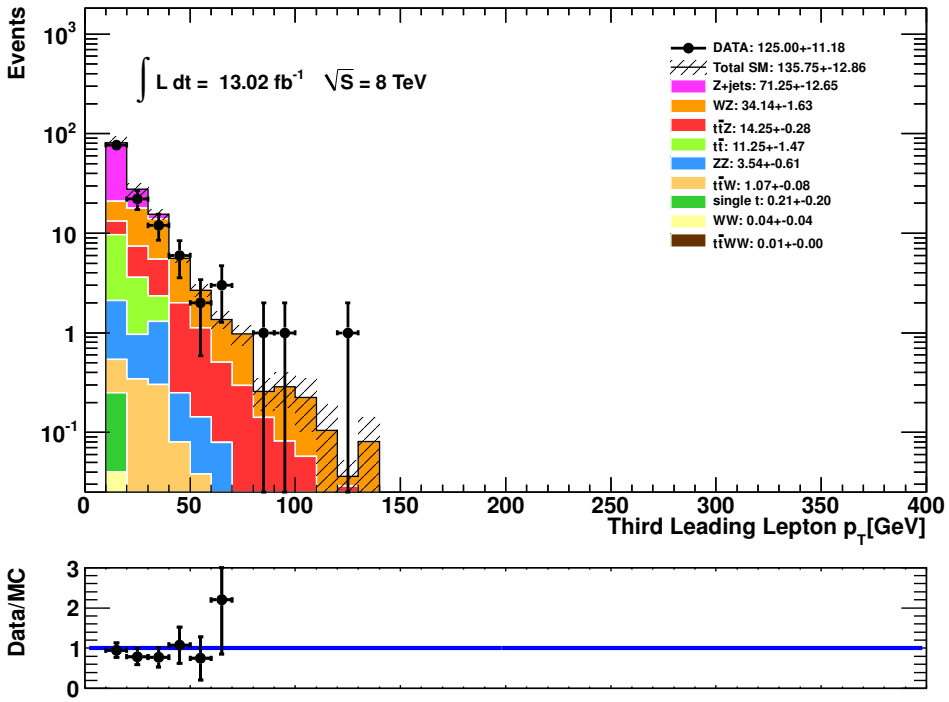

Figure 4.27: ZCR2 lepton P_T^3. Errors shown are only statistical.

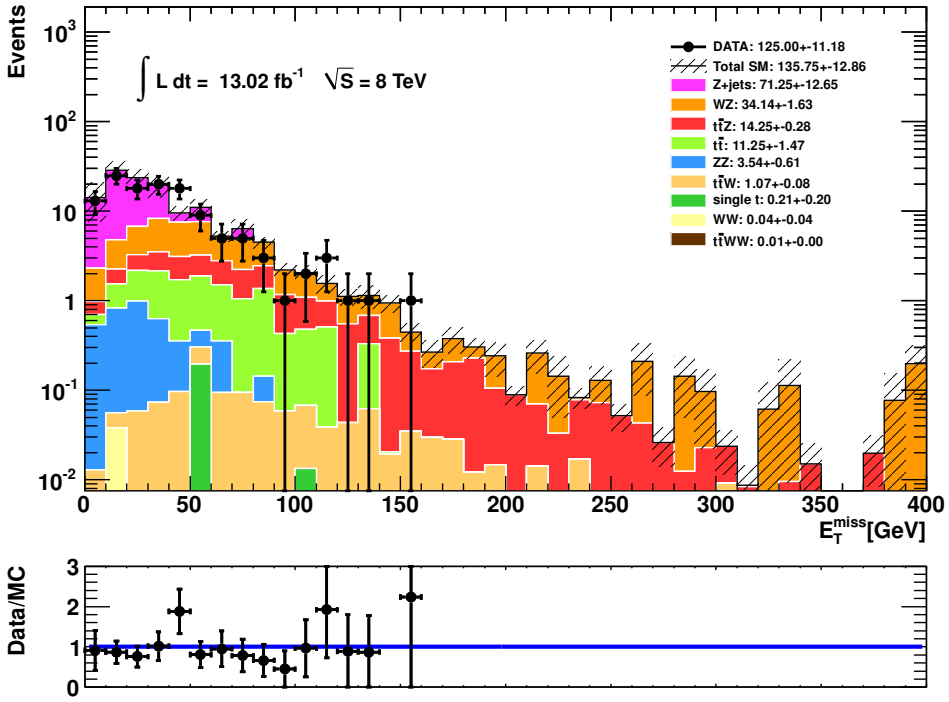

Figure 4.28: ZCR2 E_T^{miss}. Errors shown are only statistical.

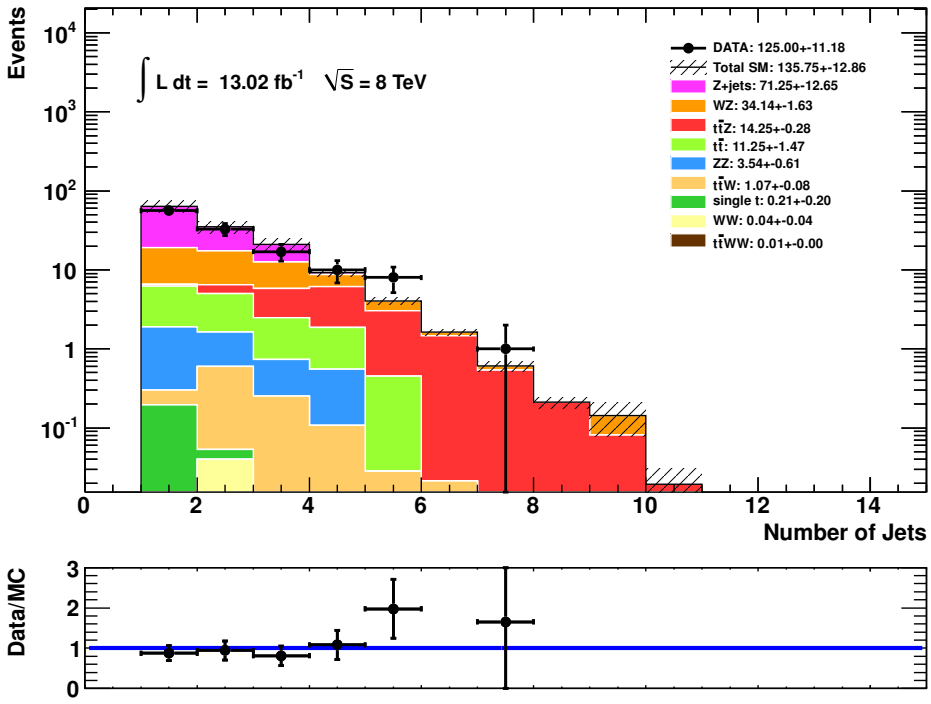

Figure 4.29: ZCR2 number of jets. Errors shown are only statistical.

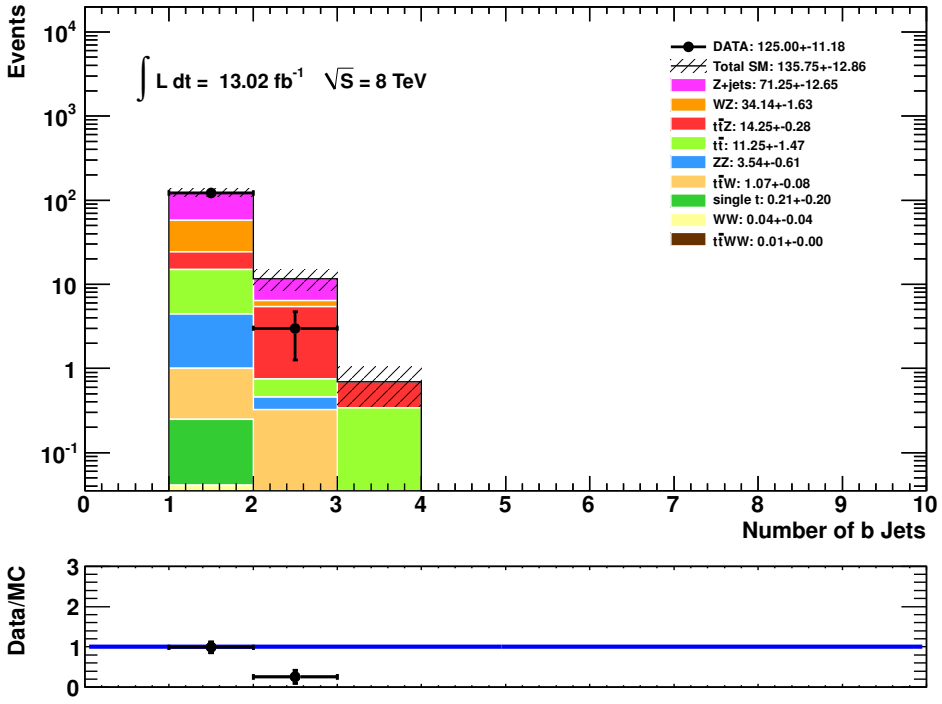

Figure 4.30: ZCR2 number of b jets. Errors shown are only statistical.

4.5 Systematic Uncertainties

Several sources of systematic uncertainty affect the predicted number of simulated signal and background events. The impact on the number of expected events is determined by varying a given systematic between extremes ($\pm$ 1σ). Several sources of systematics have been studied and listed below.

4.5.1 Lepton Trigger, Reconstruction and Identification

There are small uncertainties associated with the lepton trigger, reconstruction and identification efficiencies.

4.5.2 Jet Energy Scale

The uncertainty due to the Jet Energy Scale [34] is evaluated by shifting up and down the energy of all the jets in the simulated samples by a p_T and η-dependent fraction for jets with 15 GeV$< p_T <$ 7 TeV and $|\eta| < 4.5$. The uncertainty is applied to both the relevant objects in the event and to the corresponding components of the E_T^{miss}.

4.5.3 Jet Energy Resolution

To determine the uncertainty due to Jet Energy Resolution, the p_T of each jet is smeared according to a Gaussian distribution, with unit mean and a width given by a p_T and η-dependent resolution function [35].

4.5.4 Electron Energy

The Electron Energy Scale and the Electron Energy Resolution are found using a E_T and η-dependant function selecting Z and W events in data and J/ψ events for low-p_T electrons. The uncertainty is applied to both the relevant objects in the event and to the corresponding components of the E_T^{miss}.

4.5.5 Luminosity

The luminosity uncertainty for 2012 data is 3.9%.

Table 4.5 reports the absolute effect on the numbers of events of SM background as the uncertainties considered are varied between extremes ($\pm 1\sigma$). In this analysis due to low statistics in Sherpa ZZ samples, diboson processes were generated with Powheg for systematics studies.

The jet energy resolution and jet energy scale should have a similar effect on $t\bar{t}$, $t\bar{t}Z$ and $t\bar{t}W$ samples. Therefore having one of them several times higher than another is unreasonable. As a result due to higher statistics in $t\bar{t}Z$ samples, we have used the $t\bar{t}Z$ systematic uncertainty values for $t\bar{t}$ and $t\bar{t}W$ samples.

	$t\bar{t}Z$	WZ	ZZ	$t\bar{t}W$	$t\bar{t}$
Electron energy scale	-1,+0%	-0,+0%	-0,+0%	-0,+0%	-0,+0%
Electron energy ratio	-0,+0%	-0,+0%	-0,+0%	-0,+0%	-0,+0%
Jet energy scale	-3,+0%	-12,+9%	-16,+0%	-7,+0%	-0,+49%
Jet energy resolution	-1,-1%	+8,+8%	+16,+16%	-7,-7%	+32,+32%
Trigger	-0,+0%	-0,+0%	-0,+0%	-0,+0%	-0,+0%
Electron ID/reconstruction efficiency	-4,+0%	-4,+0%	+0,+0%	-7,+0%	-0,+9%
Muon ID/reconstruction efficiency	-1,+0%	-2,+0%	-0,+0%	-0,+0%	-0,+0%
Luminosity	-4,+4%	-4,+4%	-4,+4%	-4,+4%	-4,+4%
Total	-6.6,+4.1%	-15.6,+12.7%	-23.0,+16.5%	-12.8,+8.1%	-32.2,+59.3%

Table 4.5: The effect of the considered systematics on SM event numbers in the signal region is listed in %.

Chapter 5

Results

Applying the full event selection, as described in Section 4, a total of 13.0 events is observed in the data, compared to an expected event yield of 11.37 ± 0.65 (stat) $^{+0.59}_{-0.66}$ (sys), with an expected background contribution of 4.05 ± 0.62 (stat) $^{+0.40}_{-0.49}$ (sys) events and 7.32 ± 0.20 (stat) $^{+0.30}_{-0.48}$ (sys) signal events. The statistical uncertainties on the MC prediction is due to limited MC statistics. We see 8.95 ± 0.62 (stat) $^{+0.37}_{-0.59}$ (sys) signal events above background. The $t\bar{t}Z$ production cross section is calculated using:

$$\sigma = \frac{N_{data} - N_{bkg}}{\epsilon_{MC} \times BR \times L} \tag{5.1}$$

where $L = 13.02$ fb^{-1} is the integrated luminosity of the analysed dataset and $BR = 0.0244$ is the branching ratio of the three lepton decay channel. $\epsilon_{MC} = \epsilon \times A = 0.119$ is obtained using the MC samples, where A is the geometrical acceptance and ϵ is the efficiency of detection. The geometrical acceptance is defined as the ratio of the number of events having 3 leptons with $P_T > 10$ GeV, $\eta < 2.47$ and jets with $P_T > 20$ GeV, $\eta < 2.47$ to the number of events having only 3 leptons. There are no requirements on the number of jets, however if there is a jet in an event, it has to pass the P_T and η cuts.

The $t\bar{t}Z$ MC is leading order, but we also estimate the NLO correction. We scale the number of events given by the LO MC to the NLO cross section to get a total cross section of 208 ± 21 fb. Scaling the MC cross section by the ratio of the number of signal events observed to the number of signal events expected gives $\sigma_{t\bar{t}Z} = 254 \pm 104$ (stat) ± 13 (sys) fb. Interpreting the excess using the ϵ_{MC} from MC and BR from the Particle Data Group gives $\sigma = 237 \pm 97$ (stat) ± 12 (sys) fb.

Uncertainties in the cross sections are correlated, therefore the difference in σ is significant. This difference is not understood. It is due to a difference in the number of $t\bar{t}Z$ and $t\bar{t}Zj$ trilepton events at the generation stage from a calculated value using the trilepton BR. We have not been able to resolve this difference. A ϵ_{MC} value of 0.111 would account for the difference in the

cross section, therefore we include this as a 7% systematic uncertainty on the ϵ_{MC}.

The uncertainty on the cross section is calculated using

$$\delta\sigma = \sigma\sqrt{\frac{\delta N_{data}^2 + \delta N_{bkg}^2}{(N_{data} - N_{bkg})^2} + (\frac{\delta L}{L})^2 + (\frac{\delta \epsilon_{MC}}{\epsilon_{MC}})^2}. \tag{5.2}$$

This uncertainty on the cross section does not include any correlation between backgrounds or backgrounds and signal.

Chapter 6

Summary and Conclusion

The first measurement of $t\bar{t}Z$ production cross section to date in final states with three leptons is performed using 13.0 fb^{-1} of 8 TeV proton-proton collision data collected with the ATLAS detector at the LHC. Only final states with three leptons are considered, in which the Z boson decays to a pair of leptons and one of the W bosons coming from $t \to bW$ decays gives rise to a lepton after decay. An excess of 8.95 ± 0.62 (stat) $^{+0.37}_{-0.59}$ (sys) events above background is observed with a significance of 3.64 standard deviations above zero. We have assumed no statistical error on the acceptance or efficiency of detection. The measured $t\bar{t}Z$ cross section is $\sigma_{t\bar{t}Z} = 254 \pm 104$ (stat) $\pm$ 19 (sys) fb. It is consistent with the NLO predictions of 208 ± 21 fb [15] [16] within uncertainties.

Bibliography

[1] The ATLAS Collaboration. The ATLAS experiment at the CERN Large Hadron Collider. *J Instrum*, 3(S08003), 2008.

[2] CDF Collaboration. Observation of top quark production in pp collisions with the collider detector at Fermilab. *Phys. Rev. Lett.*, 74(14): 2626–2631, 1995.

[3] D0 Collaboration. Observation of the top quark. *Phys. Rev. Lett.*, 74: 2632–2637, 1995.

[4] D. Chakraborty, J. Konigsberg and D. L. Rainwater. Top-quark physics. *Ann. Rev. Nucl. Part. Sci.*, 53:301–351, 2003.

[5] R. S. Chivukula, S. B. Selipsky and E. H. Simmons. Nonoblique effects in the Z b anti-b vertex from ETC dynamics. *Phys. Rev. Lett.*, 69: 575–577, 1992.

[6] C. Berger, M. Perelstein, and F. Petriello. Top quark properties in little Higgs models. Technical Report SLAC-PUB-11589, 2005. URL `http://arxiv.org/abs/hep-ph/0512053`.

[7] U. Baur, A. Juste, L. Orr and D. Rainwater. Probing electroweak top quark couplings at hadron colliders. *Phys. Rev.*, D71(054013), 2005.

[8] Search for $t\bar{t}Z$ production in the three lepton final state with 4.7 fb^{-1} of $\sqrt{s} = 7$ TeV pp collision data collected by the ATLAS detector. Technical Report ATLAS-CONF-2012-126, CERN, 2012.

[9] Measurement of the associated production of vector bosons with top-antitop pairs at 7 TeV. Technical Report CMS-PAS-TOP-12-014, CERN, 2012.

[10] Peter W. Higgs. Spontaneous symmetry breakdown without massless bosons. *Phys. Rev*, 145:1156–1163, 1966.

[11] M. Kobayashi and T. Maskawa. CP-Violation in the renormalizable theory of weak interaction. *Prog. Theor. Phys.*, 49:652–657, 1973.

[12] M. Jezabek and J. Kuhn. QCD corrections to semileptonic decays of heavy quarks. *Nucl. Phys*, B 314(1):1–6, 1989.

[13] A. Quadt. Top quark physics at hadron colliders. *EPJ*, C 48:835–1000, 2006.

[14] K. Nakamura *et al.* The review of particle physics. *J. Phys. G: Nucl. Part. Phys.*, 37(075021), 2011.

[15] Kardos, Adam and Trocsanyi, Zoltan and Papadopoulos, Costas. Top quark pair production in association with a Z-boson at NLO accuracy. *Phys. Rev.*, D85(054015), 2012.

[16] J. M. Campbell and R. K. Ellis. $t\bar{t}W^{\pm}$ production and decay at NLO. *JHEP*, 1207(052), 2012.

[17] E.D. Bloom *et al.* High-Energy inelastic e-p scattering at 6° and 10°. *Phys. Rev. Lett.*, 23:930, 1969.

[18] Charles Hill. The CERN hadron ion sources, Retrieved March 2013. URL `http://linac2.home.cern.ch/linac2/sources/source.htm`.

[19] CERN. Technicalities for medium, Retrieved March 2013. URL `http://twiki.cern.ch/twiki/bin/viewauth/AtlasProtected/TechnicalitiesForMedium1`.

[20] M. Cacciari, G. P. Salam, G. Soyez. The anti-kt jet clustering algorithm. *JHEP*, 063(04), 2008.

[21] Commissioning of the ATLAS high-performance b-tagging algorithms in the 7 TeV collision data. Technical Report ATLAS-CONF-2011-102, CERN, 2011.

[22] Properties of jets and inputs to jet reconstruction and calibration with the ATLAS detector using proton-proton collisions at $\sqrt{s} = 7$ TeV. Technical Report ATLAS-CONF-2010-053, CERN, 2010.

[23] M. L. Mangano *et al.* ALPGEN, a generator for hard multiparton processes in hadronic collisions. *JHEP*, 0307(001), 2003.

[24] S. Frixione and B. R. Webber. The MC@NLO 3.2 event generator. Technical Report CERN-PH-TH/2006-012, 2006. URL `http://arxiv.org/abs/hep-ph/0601192`.

[25] G. Corcella, I. Knowles, G. Marchesini, S. Moretti, K. Odagiri *et al.* HERWIG 6.5: an event generator for Hadron Emission Reactions With Interfering Gluons (including supersymmetric processes). *JHEP*, 0101 (010), 2001.

[26] J. Butterworth, J. R. Forshaw and M. Seymour. Multiparton interactions in photoproduction at HERA. *Z. Phys. C*, 72:637–646, 1996.

[27] J. Alwall *et al.* MadGraph/MadEvent v4: the new web generation. *JHEP*, 09(028), 2007.

[28] T. Sjostrand, S. Mrenna and P. Z. Skands. PYTHIA 6.4 physics and manual. *JHEP*, 05(026), 2006.

[29] CERN. Efficiency measurements, Retrieved March 2013. URL `http://twiki.cern.ch/twiki/bin/view/AtlasProtected/EfficiencyMeasurements`.

[30] A.Ahmad *et al.* Measurement of the cross-section for jets produced in association with a W-boson in pp collisions at $\sqrt{s} = 7$ TeV. Technical Report ATL-PHYS-INT-2011-020, CERN, 2011.

[31] ATLAS Collaboration. Expected performance of the ATLAS experiment - Detector, Trigger and Physics. Technical Report CERN-OPEN-2008-020, December 2005. URL `http://arxiv.org/abs/0901.0512`.

[32] CERN. MCP analysis guidelines, Retrieved March 2013. URL `http://twiki.cern.ch/twiki/bin/view/AtlasProtected/MCPAnalysisGuidelinesRel15`.

[33] Muon momentum resolution in first pass reconstruction of pp collision data recorded by ATLAS in 2010. Technical Report ATLAS-CONF-2011-046, CERN, 2011.

[34] CERN. Jet missing energy data analysis recommendation, Retrieved March 2013. URL `http://twiki.cern.ch/twiki/bin/view/AtlasProtected/JetEtmissDataAnalysisRecommendationSummer2010`.

[35] Jet energy resolution and selection efficiency relative to track jets from in-situ techniques with the ATLAS detector using proton-proton collisions at a center of mass energy $\sqrt{s} = 7$ TeV. Technical Report ATLAS-CONF-2010-054, CERN, 2010.